PROPAGATION AND CONTROL OF BROADBAND OPTICAL AND RADIO

FREQUENCY SIGNALS IN COMPLEX ENVIRONMENTS

A Dissertation

Submitted to the Faculty

of

Purdue University

by

Bohao Liu

In Partial Fulfillment of the

Requirements for the Degree

of

Doctor of Philosophy

May 2019

Purdue University

West Lafayette, Indiana

THE PURDUE UNIVERSITY GRADUATE SCHOOL
STATEMENT OF DISSERTATION APPROVAL

Prof. Andrew M. Weiner, Chair

  School of Electrical and Computer Engineering

Prof. Daniel S. Elliot

  School of Electrical and Computer Engineering

Prof. Mark R. Bell

  School of Electrical and Computer Engineering

Prof. Meng Cui

  School of Electrical and Computer Engineering

Approved by:

  Prof. Pedro Irazoqui

    Head of the School Graduate Program

To the memory of my grandmother, Shuangzhu Fu (1928 - 2015)

ACKNOWLEDGMENTS

First and foremost, I would like to express my deep appreciation for my advisor Prof. Andrew Marc Weiner for his encouragement, patience, and guidance throughout my PhD years. Thank you Prof. Weiner for offering me an opportunity to be a member of a such amazing research team at Purdue University. What I learned from him has shaped my mind and action both professionally and personally. Just like a Chinese idiom, one day as a teacher, father for life. Many small moments will fade away as time goes by, but for sure I will remember the moments in Prof. Weiners Ultrafast optics class, how he used simple drawings to explain the evolution of the complicated mode locking differential equations and to unveil the physical meaning behind each mode locked laser component in such a mastered way. All of these moments reflect his deep understanding of the field and his thorough preparation to every instructional lecture and presentation, which states his experience as a pioneer himself in his professional area. I wish after five-year of close observation and learning, I can master my expertise in my future professional area and have a committed but joyful life as well as he does, to reach his expectation and make him proud of me.

Besides my advisor, I would like to thank Prof. Daniel S. Elliott, Prof. Mark R. Bell and Prof. Cui Meng for serving my doctoral advisory committees. I would like to thank Prof. Elliott for his experienced lectures and discussion in fundamental electromagnetic theory, Prof. Bell for his lectures in antenna theory and valuable discussion in wireless signal transmission and processing, and finally Prof. Cui for his helpful instruction and suggestion on algorithm of optical phase retrieval.

My sincere thanks also extend to the Purdue ultrafast optics family. Without our lab manager Dr. Daniel E. Leairds superb and versatile engineering skill, it would not have been possible for me to achieve my research results. He defines the word engineer and sets up the role model for us young fellow engineers to follow. I also want

to send my heartful appreciation to former group member Prof. Chen-Bin Huang. He was the one who introduced me to the field of pulse shaping and ultrafast optics when I was an exchange student at National Tsing Hua University back in 2011 and referred me this opportunity to study in this group. I would like to thank former group member Prof. V. R. Supradeepa for equipment help and valuable discussion at the beginning of my PhD career to kick off my experiments. Thanks to senior group member Prof. Yihan Li, Dr. Amir Rashidinejad and Dr. Yang Liu for the help and mentoring on my experiments. Thanks to former and present group member Dr. Jian Wang, Dr. Andrew J. Metcalf, Dr. Joseph Lukens, Dr. Pei-Hsun Wang, Dr. Xiaoxiao Xue, Dr. Chengying Bao, Dr. Justin Wirth, Dr Dennis Lee, Mr. Steven Chen, Mr. Abudulla Al Noman, Dr. Javier Valderrama, Dr. Hyoung-Jun Kim, Dr. Ryo Suzuki, Mr. Prangjnesh Reddy, Mr. Beichen Wang, Mr. Sebastian Ortega, Ms. Cong Wang, Mr. Ziyun Kong, Mr. Mohammed Saleh Al alshaykh, Mr. Keith McKinzie, Mr. Hsuan-Hao Lu, Ms. Alex Moore, Mr. Navin Lingaraju, Mr. Nathan OMalley, and Ms. Suparna Seshadri for helpful technique discussions or collaborations. I also want to thank Prof. Jin-Wei Shi and Dr. Jhih-Min Wun from National Central University, Taiwan for our pleasant collaborations. Special acknowledgement to Dr. Jose Jaramillo, Dr. Ogaga Daniel Odele, Dr. Poolad Imany and Mr. Oscar Eric Sandoval who all joined the group around the same time with me. All the friendship we built up over the years is of great value. I would also like to thank all the students who were in my undergraduate optics lab courses when I was serving as the lab instructor. I also learned a lot through such teaching experience and it indeed benefits my PhD journey.

Finally, I want to express my gratitude to my family and friends. Their unconditional support helped me in every kind of situation. And I want to send my most truthful thank to my mother Xiangping Gao and father Lifeng Liu, for everything they have done for me.

TABLE OF CONTENTS

LIST OF TABLES

LIST OF FIGURES

Figure   Page

Figure   Page

ABBREVIATIONS

AWG   arbitrary waveform generator (generation)

CW   continuous-wave

FPGA   field-programmable gate array

FTM   frequency-to-time mapping

MMF   multimode fiber

PC   phase conjugation (compensation)

PPLN   periodically poled lithium niobate

RF   radio-frequency

Rx   receiver

SHG   second-harmonic generation

SMF   single-mode fiber

TR   time-reversal

Tx   transmitter

ABSTRACT

Liu, Bohao Ph.D., Purdue University, May 2019. Propagation and Control of Broadband Optical and Radio Frequency Signals in Complex Environments. Major Professor: Andrew M. Weiner.

A complex environment causes strong distortion of the field, inhibiting tasks such as imaging and communications in both the optical and radio-frequency (RF) region. In the optical regime, strong modal dispersion in highly multimode fiber (MMF) results in a scrambled output field in both space (intensity speckles) and time (spectral and temporal speckles). Taking advantage of the pulse shaping technique, spatial and temporal focusing has been achieved in this thesis, offering potential opportunities for nonlinear microscopy and imaging or space-division multiplexed optical communication through MMF. In the RF regime, multipath effect in wireless RF channel gives multiple echoes with random delay and amplitude attenuation at the receiver end. Static channel sounding and compensation with ultra-broadband spread spectrum technique resolves the issue by generating a peaking signal at the receiver, significantly improving the signal-to-noise/interference performance. However, the limited communication speed in the static approach makes it challenging for sounding and compensation in a dynamic channel. Here, we achieve real-time channel sounding and compensation for dynamic wireless multipath channel with 40 μs refresh rate by using a fast processing field programmable gate array (FPGA) unit, providing potential opportunities for mobile communications in indoor, urban, and other complex environments. Furthermore, by combining broadband photonics and RF radar technologies, a high depth and transverse resolution wide bandwidth (15 GHz) W-band (75 - 110 GHz) photonic monopulse-like radar system for remote target sensing is demonstrated, offering prospects for millimeter wave 3-D sensing and imaging.

1. INTRODUCTION

Can we see through and communicate through a complex scattering environment? The answer is more than 'yes.' It turns out that the complexity gives us more powerful 'eyes' and 'ears' than what a transparent world offers. We are not simply seeing and communicating through the complex scattering environment, but seeing and communicating more securely with significantly enlarged channel throughput. In the field of optics, research interest in multimode fiber (MMF) imaging and communication has increased over the last few years. Different from the widely used standard single mode fiber (SMF), an MMF can support multiple optical modes with different propagation performances, such that each different mode families travel with different group velocities (modal dispersion). When manufactured to support numerous modes (usually done by designing a large core diameter), the field after propagating through the MMF will be distorted in space and in time with random substructures, resulting in spatial speckle patterns for single frequency input, and temporal and spectral speckles for short pulse input, which makes MMF a much more complex medium than SMF.

Similar to modal dispersion in an MMF, each scattering path in an RF wireless channel can be viewed as a guiding mode. Therefore, an radio-frequency (RF) channel with rich multipath scattering will result in a received field with random amplitude attenuation and time delay—unlike a direct RF channel with few or no scatters. For this reason, the multipath (modal dispersion) effect has become a research subject, both in RF wireless channels and in optical scattering medium. In addition to overcoming the limitation from modal distortion, utilizing the multipath randomness will be crucial to exploit the full capacity of both MMF (optical) and RF wireless channels.

In this dissertation, we will explore the multipath effects in both optical and RF domains. In optical domain, the optical pulse shaping technique for field characteriza-

tion and pulse compensation at an MMF's output surface provides us the capability to deliver ultrashort pulses through the highly scattering medium. In RF domain, using RF arbitrary waveform generation (AWG) techniques, high-speed characterization and compensation of dynamic RF wireless multipath channel is achieved, extending our work from static channel to more complicated dynamic channel. By combining the optical pulse shaping technique and traditional radar theory, we further extend our work to the W-band range (75–110 GHz). A W-band monopulse-like radar scheme is demonstrated and a photonic phase shifter is applied to generate sum and difference interference patterns over extremely wide bandwidth, up to 15 GHz. The photonic radar system is then used for high depth and transverse resolution targets detection and sensing.

The remainder of this document will be structured as follows: in Chapter 2, we will introduce a method for characterizing an MMF field at its output surface, where the optical field is scrambled both spatially and temporally by modal dispersion; in Chapter 3, we discuss the multipath effects in RF wireless channels and will demonstrate an scheme for sounding and compensating dynamic channel links; in Chapter 4, we discuss the W-band monopulse-like radar system with ultrabroad bandwidth via photonic assisted AWG; in Chapter 5, we discuss the experimental demonstration of the W-band photonic radar in a high resolution remote targets sensing system: and in Chapter 5, we review the accomplished work and point the future research directions for each topic.

1.1 Space-Time Focusing in a Highly Multimode Fiber via Optical Pulse Shaping

Scattering of waves has been extensively studied in RF wireless transmission [1–3] and acoustics [4–6], for which direct time domain measurements are possible. In optics, direct measurements of the field are ruled out due to the much higher frequencies. However, it is well known that strong distortion of the optical wavefront results

in a noise-like field, with intensity speckle patterns in space in the case of a single-frequency input light [7]. Taking advantage of spatial light modulator technologies, wavefront shaping [8–12] has been applied to overcome spatial distortions in strongly scattering bulk materials, thereby achieving spatial control of the diffusive light. For the case of broadband input light, speckle also arises in time and frequency; different random substructures in the time and frequency dimensions are seen at each specific output location [13, 14]. The intensity correlation of speckle patterns with frequency has been studied for characterization of the scattering impulse response [15, 16]. Experiments in [17–20] demonstrated spatiotemporal focusing of ultrafast pulses through bulk scattering medium via wavefront shaping techniques. Such experiments open up possibilities for enhancing two-photon nonlinear processes and improving microscopy in turbid samples.

Propagation through multimode fibers (MMF) can also lead to speckle-like phenomena in space, frequency, and time. Here, the distortions arise from the superposition of different guided modes and modal dispersion. Aside from their traditional use for short distance communication links, MMFs have received significant recent research attention for coherent image transmission [21, 22], mode-division multiplexing for high speed optical communications [23, 24], quantum research [25], and multimode complex nonlinear optics [26–28]. Overcoming and utilizing speckle-like distortions caused by modal dispersion scattering in MMFs is of interest for such applications. Inspired by wavefront shaping experiments in bulk scattering materials, spatial focusing through MMF has been achieved using wavefront shaping controlled by different methods such as transmission matrix measurements [25, 29, 30] and optical phase conjugation [31]. This has led to a potential for medical-use endoscopes with improved resolution and compactness, and with all-optical (vs. mechanical) scanning control. In connection with broadband light, correlation techniques have been used to study the frequency dependence of intensity speckle patterns at the output of MMFs, and to realize a MMF-based spectrometer [32, 33]. Techniques for characterizing the time domain output of MMFs illuminated by ultrashort pulses input were reported

in [34, 35]. In [36, 37], ultrashort pulses were delivered through MMF via a wavefront shaping technique, in which short pulses transmitted through and distorted by the MMF interfere with an ultrashort reference pulse to form a time-gated digital hologram containing spatial phase information. The short pulses were delivered by the spatially shaped reference counterpropagating through the same MMF with spatial mode-selective phase conjugation process. Such work has promise for nonlinear optical imaging through fiber and may have relevance for optical communications in MMF.

Here, for the first time to our knowledge, we perform reference-free characterization of spectral and temporal speckles at different spatial positions on the output face of a MMF, and achieve space-time focusing involving all the excited propagating modes. Transform limited pulses are formed locally at the MMF output by compensating the spectral phase response via optical pulse shaping [38, 39]. The concept is analogous to our group's work on temporal shaping of ultrawideband RF wireless signals for temporal and spatial focusing in strong multipath channels [40], but now extended for the first time into the optical regime.

1.2 Ultrabroadband RF Wireless Multipath Channel

For wireless RF communication, the link performance depends heavily on the propagation channel. In indoor, urban, or other cluttered environments, the channel is usually dominated by multipath [41]; that is, the transmitter and receiver are connected by a large number of scattering and multiple reflection paths of different lengths. In the time domain, the received signal consists of a large number of apparently random short echoes, which have delays and attenuation due to the paths they took in their propagation from the transmitter (Tx) to the receiver (Rx). In the frequency domain, the impulse channel response is highly structured, including a multiple of apparently random deep fades. Moreover, the detailed substructures of the channel response in the time and frequency domains vary rapidly with displace-

ment of the antennas, hence leading to the topic of spatial and temporal channel characterization and focusing.

The recent emerging Ultrawideband (UWB) technology [1] is an effective solution to the multipath problem due to the large frequency bandwidth compared to conventional narrowband systems. The detailed structure of a channel response in the frequency domain is proportional to the inverse of the delay spread (hundreds of nanoseconds). That is, a UWB system with several GHz bandwidth is fine enough to resolve the multipath components at the receiver. Combining signal processing and arbitrary waveform generation (AWG) techniques, the multipath channel can be characterized (channel sounding) and compensated, which states the multipath immunity of the UWB system. Besides, UWB also provides other significant advantages such high data rates (RF link capacity grows linearly with increasing bandwidth) [42], high precision for location and ranging applications (high temporal resolution and ranging resolution) [43].

Static channel characterization (channel sounding) and compensation of a UWB multipath channel has been achieved in our group's previous experiments with different AWG schemes (electronics and photonics) [40, 41, 44–47]. In channel sounding, a spread spectrum linear chirp signal is broadcast by Tx and a received signal is recorded at Rx. The channel response is then calculated by deconvolution. The measured channel response from the channel sounding process is then used to calculate the precompensation waveform for transmission. The transmitted precompensation will self-compress after propagating in the multipath wireless channel from Tx to Rx. The channel compensation gives a strongly peaked, bandwidth limited short pulse signal at Rx, which significantly enhances the peak-to-average power ratio and the signal-to-noise/interference. Notably, because the channel response varies rapidly with location, a compensation waveform is unique to a certain Tx-Rx location pair, bringing up new potentials for selective or covert transmission. However, the strong spatial dependence of the channel response gives rise to challenges for dynamic channels involving mobile antennas or a time-varying environment.

In this work, channel sounding and compensation for dynamic channel with 40 μs update rate is achieved. Our approach implements spread spectrum channel sounding on an electronic processing unit comprising of fast analog-to-digital (AD) and digital-to-analog (DA) converters tightly coupled to a high-end field-programmable gate array (FPGA). The approach with the FPGA eliminates unavoidable latency and communications bottlenecks with general-purpose test equipment such as arbitrary waveform generators and oscilloscopes. With 6 GHz total bandwidth and $\sim 30\mu s$ processing time, our platform offers potential opportunities for enhanced performance (signal-to-noise/interference, covertness potential) of mobile or dynamic broadband RF signaling over multipath channels.

1.3 Ultra-Broadband Photonic Monopulse-Like Radar for Remote Sensing

The research related to millimeter wave (MMW) and subterahertz (sub-THz) has developed significantly in recent decades. Besides circumventing the congestion of lower radio-frequency (RF) bands, higher frequency RF regions offer access to broader bandwidths for applications such as ultrahigh-speed wireless communication [48–53], high-resolution ranging [54–56], and electromagnetic imaging [57, 58]. Also, conventional imaging and sensing systems working in the frequency region below 30 GHz require large apertures [59], making tasks such as small target detection and high resolution imaging problematic, requiring more complicated systems like synthetic aperture radar (SAR) to improve performance [60, 61]. However, the update rate will be affected by the motion speed of the SAR system. In the MMW region from 30 to 300 GHz (1 cm to 1 mm), a small aperture inherited from the small wavelength combined with high depth resolution provided by the ultra-broad bandwidth makes it competitive in important applications such as personnel screening [54], self-driving vehicles [62], and intelligent driver assistance systems [63]. To further attain high angular resolution for high resolution 3-dimensional (3-D) imaging, the quasi-

optics approach based on MMW/THz lens and parabolic mirror has been demonstrated [54,55,64]. In this approach, the MMW beam is focused, hence increasing the transverse resolution. However, the working distance with high transverse resolution is limited due to focusing. Monopulse radar is a more effective solution to enhance transverse spatial resolution while keeping the working distance only affected by system signal-to-noise ratio (SNR) [63,65]. Previously widely demonstrated and applied in monopulse tracking [66,67] in traditional radar systems, beamforming in monopulse radar switches between sum and difference far-field pattern of a simple transmitter array (two/four elements for transverse spatial resolution in one/two dimensions), in which a sharp destructive null is obtained in the center for difference pattern and a constructive peak is obtained for sum pattern. It is worth mentioning here, difference pattern is the key to detecting the sign of angular displacement in a tracking system, hence emphasizing the importance of the phase shifter in a monopulse radar system. However, the traditional electronic MMW phase shifter, which is the essential part to generate and switch between sum and difference pattern, has difficulty handling ultra-broadband waveforms, bringing difficulty to the high transverse monopulse system for acquiring high depth resolution. Photonic beamforming with true time delay (TTD) is an alternative solution to eliminate the pulse distortion and frequency(time) dependent far-field patterns (the squint phenomenon) that arise in transmitter arrays with traditional phase shifters. It has been demonstrated in phase array antenna systems [68, 69] but again with limited bandwidth (up to 1 GHz). The limitation for attaining a high resolution 3-D sensing system now breaks down to the lack of versatile ultrabroadband waveform generation and phase shifting.

The recently developed photonic-assisted arbitrary waveform generation (AWG) technique [70, 71] has paved the way for versatile RF-AWG both at baseband frequencies [72–76] and at frequencies extending to the low MMW region [3, 77]. Such photonic approaches also provide notable advantages against traditional electronic approaches with high bandwidth, low timing jitter and phase-noise performance [78, 79], immunity to electro-magnetic interference (EMI), cost-effective and low propagation

loss radio-over-fiber (RoF) signal distribution [80]. By applying the optical pulse shaping technique incorporated with frequency-to-time mapping (FTM) theory [3,38], combined with the state of art high-power near-ballistic uni-traveling-carrier photodiode (NBUTC-PD) based photonic transmitter-mixer (PTM) [81], high quality waveforms with large bandwidth-to-time product can be generated and transmitted in a MMW radar system. In this work, build up from our group's previous achieved high resolution ranging system [56] in W-band (75 - 110 GHz), an ultrabroad bandwidth photonic monopulse radar system with 15 GHz bandwidth (80 - 95 GHz) has been demonstrated. Beamforming of sum and difference patterns are achieved and a remote sensing system for multiple targets detection with high ranging and transverse resolution is demonstrated. To the best of our knowledge, this is the first demonstration of a ultra-broad bandwidth monopulse-like photonic radar system.

2. MMF CHARACTERIZATION AND PULSE COMPENSATION

2.1 MMF Background

Highly multimode fibers support a large number of propagating modes. From geometrical-optics point of view, different ray traces propagate through the fiber with various angles to the axis of the guide. Therefore, the travelling lengths of the rays vary with the angles of propagation, which results in different path delays as they travel from fiber input to output. Other than the geometrical-optics approach, a more accurate electromagnetic analysis by solving Maxwells equations [84] for an MMF system can be performed. The multiple solutions to the equations show there are multiple modes propagating, each with a different group velocity. By either argument, the optical field at any MMF ouput surface point is a sum of multiple individual contributions. Given a long enough path difference (more than 2π) and a coherent enough input source, the highly structured interference effects will be observed in the intensity distribution across the end of the guide (speckle pattern). Figure 2.1(a) shows an example of a speckle pattern at the MMF end surface. A highly multimode fiber (Thorlabs FG200LCC) with $200\mu m$ core diameter is used. For input coupling, the collimated light is focused into the MMF in free space by a lens. At the output, a speckle pattern is recorded by an infrared (IR) charged-coupled device (CCD) camera. The coherent source is a continuous wave (CW) laser that works at optical C-band (1530–1565 nm) and in this measurement, the wavelength is around 1550 nm.

Portions of the results in this chapter have been published in Refs. [82] and [83].
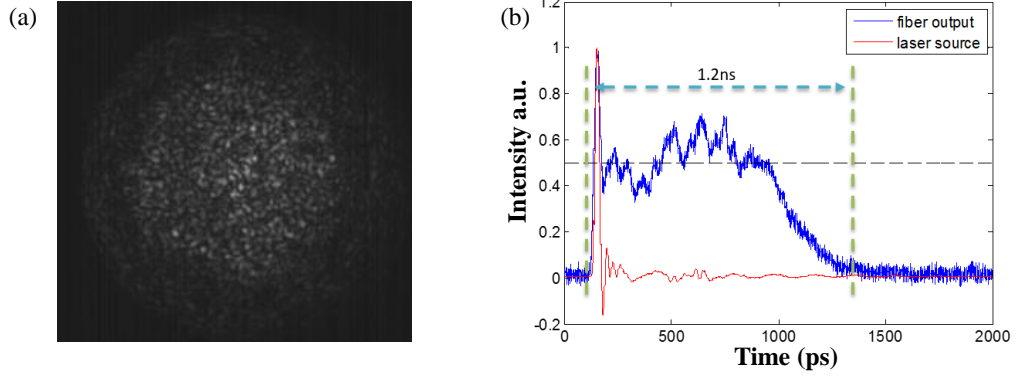
Fig. 2.1: Multimode fiber (a) speckle pattern at fiber output surface with single frequency input, and (b) time spread with broadband mode-locked laser input. Speckle pattern is acquired by an IR CCD camera and time spread is acquired by a sampling oscilloscope after photoelectric conversion by a fast photodetector. In (b), red trace is the impulse response of the photodetector with femtosecond pulse input, and blue trace is MMF time spread due to modal dispersion.

As introduced in section 1.1, the speckle pattern at the MMF output is frequency-dependent and it also decorrelates as the frequency of the input source is detuned farther away. In the time domain, the spread of time delays associated with various paths is related to the frequency dependence of the speckle pattern. Figure 2.1(b) shows the example of the time spread when the input is a broadband femtosecond source. In order to simplify the pulse measurement process for time spread observation, a 25 m MMF is used and the ~ 1 ns delay spread can be observed after photoelectric conversion using a 20 GHz photodetector (~ 50 ps response time). The goal of this experiment is to focus the light both spatially and temporally at the MMF output by characterizing the MMF impulse response and pulse compensation.

2.2 Intensity Speckle Frequency Correlation

The relation between the frequency correlations of the intensity speckles and the MMF output field temporal spread is discussed in the section. The superposition of modes at the output of a MMF gives rise to speckle effects. For sufficiently narrow-band input light, a highly structured noise-like intensity distribution may be observed
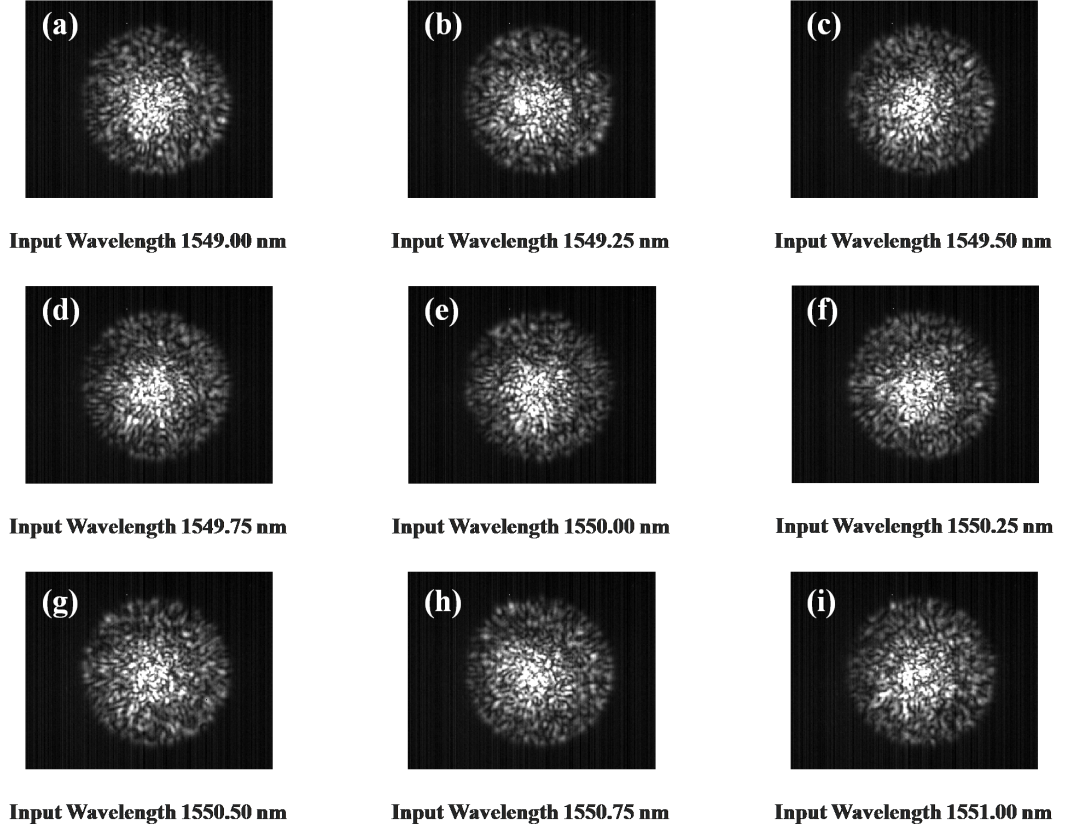
Fig. 2.2: (a) (i) Nine examples of the intensity speckle pattern at the MMF output, using a single frequency input laser and 0.25 nm wavelength steps. An animation of the MMF intensity speckle patterns with the laser stepped over a 2 nm wavelength range with 0.01 nm increments can be found in the supplementary material in [83]. The MMF fiber length is 25 meters.

across the MMF output surface [7]. Due to modal dispersion, such speckle patterns are frequency/wavelength dependent, which means different input optical wavelengths result in different MMF output intensity distributions. Figures 2.2(a) to (i) and the animation file (see Media 1 in [83]) show an example of frequency dependent intensity speckle patterns recorded using a tunable continuous wavelength (CW) laser as the input source. As discussed in [7], the frequency dependence of the speckle pattern is related to the fiber length, since the phase differences between the various MMF modes are expected to scale with the fiber length. This results in different interfer-
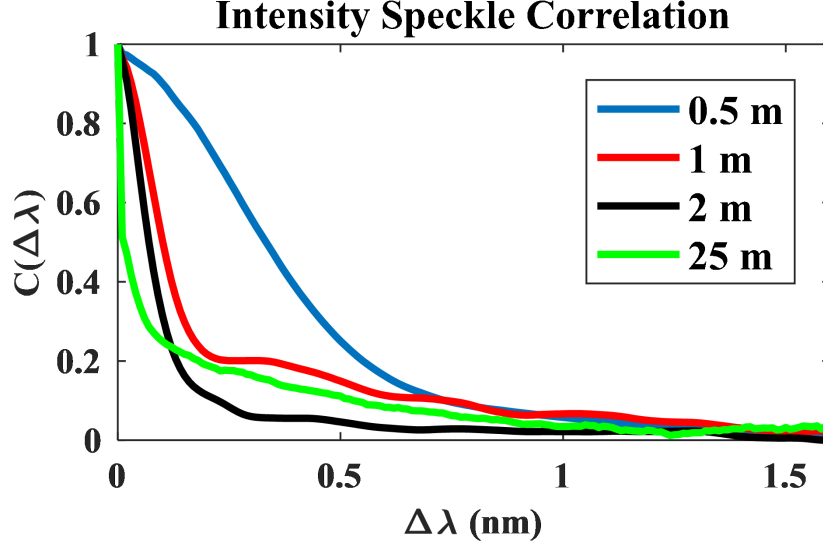
Fig. 2.3: Normalized intensity speckle correlation functions $C(\Delta\lambda)$ with different MMF fiber length.

ence structures. Likewise, the spread in the time delays is determined by the fiber length and the difference in the group velocities of the various modes. In general, the frequency-dependence of the speckle patterns can be used to estimate the delay spread of the output MMF field. In particular, the decorrelation width of the speckle in frequency (or wavelength) is inversely proportional to fiber length and the total delay spread. The intensity speckle correlation function [15, 32] is given by

$$C(\Delta\lambda) = \frac{\langle[I(\lambda) - \langle I(\lambda)\rangle][I(\lambda + \Delta\lambda) - \langle I(\lambda + \Delta\lambda)\rangle]\rangle}{\langle I(\lambda)\rangle\langle I(\lambda + \Delta\lambda)\rangle} \qquad (2.1)$$

where $I(\lambda)$ is the speckle intensity distribution at a particular wavelength λ and the angle brackets stands "$\langle\rangle$" for averaging over space.

Figure 2.3 shows the intensity speckle correlation functions for various fiber lengths. The decorrelation width at $C(\Delta\lambda) = 0.5$ is approximately 0.01 nm (1.25 GHz) for the longest (25 m) piece of MMF. The inverse of the frequency correlation width is 800 ps, which is roughly consistent with the time spread observed for the 25 m MMF shown in Fig. 2.1(b). This corresponds to 32 ps per meter. The wavelength-dependent decorrelation of the speckle patterns is also shown for shorter fiber lengths of 0.5 m, 1

m, and 2 m. Generally, we observe the expected trend: the speckle decorrelates more rapidly for longer fibers, with correlation bandwidth very roughly inversely proportional to fiber length. For example, for the 0.5 m fiber, 50% decorrelation occurs for $\Delta\lambda$ of 0.33 nm. Note however that the time spread and the correlation width are expected to depend on the spectrum of excited modes. In turn, the modes excited depend on the details of the input coupling to the MMF, which was not identical in all the measurements. Furthermore, the degree to which different spatial modes of the MMF couple with each other is also known to affect the time spread [85]. For the four fiber lengths considered here, the MMFs are necessarily wrapped in different physical forms, since the positions of the input and output coupling stages are fixed. This may also cause variation in the time spreads between MMF samples. For these reasons, the scaling of the frequency correlations shown in Fig. 2.3, and the relation between time spread reported in the following sections and frequency correlation width reported in this section, should be viewed as illustrative but not exact.

2.3 Characterization and Compensation via Pulse Shaping - Experimental Setup and Method

The experimental setup for MMF characterization and pulse compression is shown in Fig. 2.4. Unlike the speckle pattern measurements in Fig. 2.1, here we use a 1-meter length of the same MMF with a different launch condition to limit the temporal spread to below 20 ps, which fits within the time aperture of the pulse shaper (Finisar WaveShaper 1000S). A mode-locked fiber laser is used as the input optical field, with its spectrum band-pass filtered to pass 1534 1550 nm (2 THz bandwidth) in order to fit in the quasi-phase matching acceptance bandwidth of the nonlinear waveguide in the following intensity autocorrelator. (The same filtered, mode-locked fiber laser is used as the input for Fig. 2.1(b).) The distorted output field is sampled spatially by a SMF, spectral shaped by a pulse shaper, and then measured by an intensity autocorrelator. It is worth mentioning that the second harmonic generation (SHG)
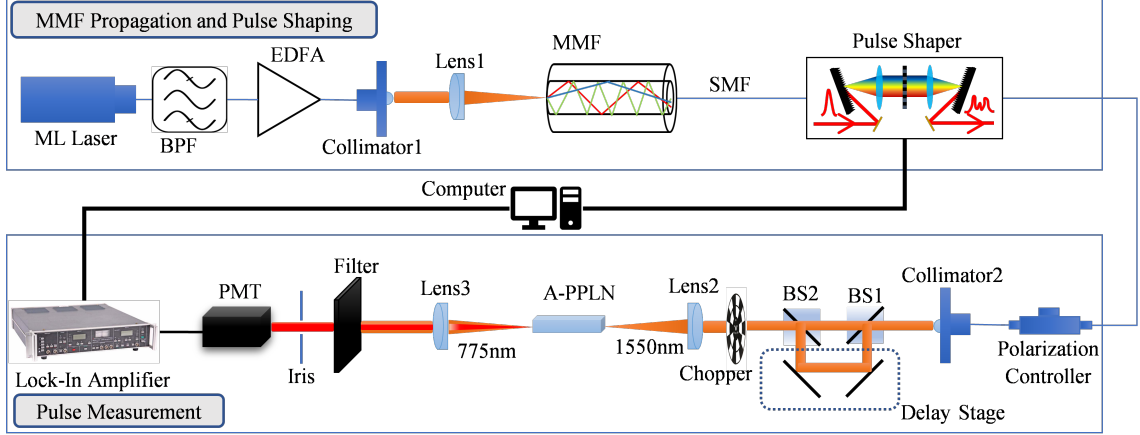
Fig. 2.4: Experimental setup of optical field characterization and pulse compensation. MMF, multimode fiber; ML laser, mode-locked laser; BPF, band pass filter; EDFA, erbium doped fiber amplifier; LCM, liquid crystal modulator; BS, beam splitter; A-PPLN, aperiodically poled lithium niobate crystal; PMT, photomultiplier tube.

in the intensity autocorrelator is achieved by using an aperiodically poled lithium niobite (A-PPLN) waveguide, offering significant advantage in the second harmonic generation sensitivity [86].

As for the characterization of the MMF impulse response at a specific output location, $H(\omega) = |H(\omega)|e^{j\phi(\omega)}$, a pulse shaping technique is applied to retrieve the spectral phase $\phi(\omega)$, and to implement spectral phase compensation, i.e., applying $[-\phi(\omega)]$ on the pulse shaper. Second harmonic generation is used to guide the phase compensation; the spectral phase is adjusted to maximize the SHG yield (either using just one arm of the autocorrelator or setting the autocorrelator delay to zero). This phase retrieval method can also be applied to other type of optical sources such as electro-optic(EO) comb [87, 88].

In detail, the spectrum of the output field is equally divided into N sections with $\omega_k = \omega_0 + (k-1)\Delta\omega$ (k is a positive integer), $N = 100$ in this experiment, in order to have fine enough spectral resolution (20 GHz, 0.16 nm) for resolving the spread in the time domain. The spectral phase is characterized section by section, starting from section 3. (Note that the spectral phase has two degrees of freedom, which define the pulses group delay and overall phase; these do not affect the pulse shape or the SHG

reading and need not be characterized for our purposes.) For example, the phase value of frequency section k, ω_k, is characterized after the phase values of previous *k-1* sections are already acquired and compensated by programming the pulse shaper, while sections *k+1* to section N are blocked. In this case, the MMF output field can be written as

$$E_{MMF} = \sum_{i=1}^{k-1} E_i e^{j\omega_i t} + E_k e^{j\omega_k t} \tag{2.2}$$

where $E_i = |E_i|e^{j\phi_i}$. In general, we write the phase at frequency ω_i as $\phi_i = \widetilde{\phi}_i + \phi_{i,shaper}$, where $\widetilde{\phi}_i$ is the phase after the fiber and $\phi_{i,shaper}$ is the phase applied by the pulse shaper. Here we take $\phi_i = 0$ for $i \leq k - 1$, which corresponds to the assumption that all frequencies $\omega_i < \omega_k$ have already been phase compensated. Assuming broadband phase matching, second harmonic intensity may be written as

$$
\begin{aligned}
I_{SHG} =& (E_{MMF}E_{MMF}^*)^2 \\
=& (\sum_{i=1}^{k-1} E_i e^{j\omega_i t} + E_k e^{j\omega_k t})(\sum_{i=1}^{k-1} E_i e^{j\omega_i t} + E_k e^{j\omega_k t}) \\
& (\sum_{i=1}^{k-1} E_i^* e^{-j\omega_i t} + E_k^* e^{-j\omega_k t})(\sum_{i=1}^{k-1} E_i^* e^{-j\omega_i t} + E_k^* e^{-j\omega_k t})
\end{aligned}
\tag{2.3}
$$

I_{SHG} can also be written as

$$I_{SHG} = I_{SHG,0} + I_{SHG}(\phi_k) \tag{2.4}$$

where $I_{SHG,0}$ term is independent of ϕ_k, and $I_{SHG}(\phi_k)$ is dependent on ϕ_k. The second-harmonic intensity signal recorded in the experiment is the time average of I_{SHG}. We write is as

$$\langle I_{SHG} \rangle = \langle I_{SHG,0} \rangle + \langle I_{SHG}(\phi_k) \rangle \tag{2.5}$$

where $\langle \cdots \rangle$ represents the time average. From Eq. 2.3, by taking terms from each bracket that are not related to ϕ_k (from frequency section 1 to $k-1$) or taking terms that can have ϕ_k cancelled out. We have

$$
I_{SHG,0} = \sum_{a=1}^{k-1}\sum_{b=1}^{k-1}\sum_{c=1}^{k-1}\sum_{d=1}^{k-1} E_a E_b E_c^* E_d^* e^{j(\omega_i+\omega_b-\omega_c-\omega_d)t}
$$
$$
+ 2|E_k|^2 \sum_{a=1}^{k-1}\sum_{b=1}^{k-1} E_a E_b^* e^{j(\omega_a-\omega_b)t} + |E_k|^4
$$

(2.6)

After time average, the fast-varying terms (any term with $e^{j\omega t}$ when $\omega \neq 0$) will be filtered out. We now have

$$
\langle I_{SHG,0} \rangle = \sum_{a=1}^{k-1}\sum_{b=1}^{k-1}\sum_{c=1}^{k-1}\sum_{d=1}^{k-1} E_a E_b E_c^* E_d^* \Big|_{a+b=c+d} + 2|E_k|^2 \sum_{a=1}^{k-1}\sum_{b=1}^{k-1} E_a E_b^* \Big|_{a=b} + |E_k|^4
$$
$$
= \sum_{a=1}^{k-1}\sum_{b=1}^{k-1} |E_a|^2|E_b|^2 + 2|E_k|^2 \sum_{a=1}^{k-1} |E_a|^2 + |E_k|^4
$$

(2.7)

It is a constant offset of the second-harmonic intensity signal $\langle I_{SHG} \rangle$. The key information is included in $I_{SHG}(\phi_k)$. From Eq. 2.3. it can be written as

$$
I_{SHG}(\phi_k) = E_k \sum_{a=1}^{k-1}\sum_{b=1}^{k-1}\sum_{c=1}^{k-1} E_a E_b^* E_c^* e^{j(\omega_k+\omega_a-\omega_b-\omega_c)t}
$$
$$
+ E_k|E_k|^2 \sum_{a=1}^{k-1} E_a^* e^{j(\omega_k-\omega_a)t} + E_k^2 \sum_{a=1}^{k-1}\sum_{b=1}^{k-1} e^{j(2\omega_k-\omega_a-\omega_b)} + c.c.
$$

(2.8)

Since $\omega_k > \omega_a$ and $2\omega_k > \omega_a + \omega_b$, after time averaging, $\langle I_{SHG}(\phi_k) \rangle$ can be written as

$$
\langle I_{SHG}(\phi_k) \rangle = E_k \sum_{a=1}^{k-1}\sum_{b=1}^{k-1}\sum_{c=1}^{k-1} E_a E_b^* E_c^* e^{j(\omega_k+\omega_a-\omega_b-\omega_c)t} \Big|_{k+a=b+c} + c.c. \qquad (2.9)
$$

Information on ϕ_k is contained in the $\langle I_{SHG}(\phi_k) \rangle$ term. Note that, the time average in Eq. 2.9 picks out frequency combinations for which $\omega_k + \omega_a - \omega_a - \omega_b = 0$. Since $\phi_i = 0$ for $i \leq k - 1$, we have

$$\langle I_{SHG}(\phi_k) \rangle = \cos \boldsymbol{\phi_k} \cdot 2|E_k| \sum_{a=1}^{k-1} \sum_{b=1}^{k-1} \sum_{c=1}^{k-1} |E_a E_b E_c| \Bigg|_{k+a=b+c} \tag{2.10}$$

Thus, the acquired SHG intensity read by the lock-in amplifier shows a simple sinusoidal dependence with respect to the phase value applied by the pulse shaper. In this experiment, 8 equally spaced phase values, between 0 and 2π, are applied on each frequency section. This results in 8 corresponding SHG intensity values which over-sample the $\cos \boldsymbol{\phi_k}$ function. Therefore, by performing an FFT of the SHG data, the MMF spectral phase response $\widetilde{\phi_k}$ can be retrieved with a resolution limited only the experimental signal-to-noise. Then the negative value of the phase retrieved is applied by the pulse shaper, ensuring that $\widetilde{\phi_k} + \phi_{k,shaper} = 0$. This finishes the kth section and we repeat this procedure for the remaining sections.

Figure 2.5 shows normalized intensity autocorrelation measurements of the output of the 1-m MMF, both with and without spectral phase compensation. The data are in close agreement with simulated results calculated from the measured power spectrum and retrieved phase information. Here the background is subtracted for display reasons. The autocorrelation in Fig. 2.5(a) has a broad envelope with a narrow spike in the middle, with a roughly 2:1 peak to envelope contrast in the background-free case (3:2:1 peak to envelope to background contrast with the background retained). This is the signature of a finite duration noise burst [89], as expected for a temporal speckle field caused by modal dispersion broadening. The 15-ps-width of the broad envelope suggests a total broadening of 10 ps. After spectral phase compensation, the output field is compressed back to the transform-limit, Fig. 2.5(b), with 2:0 autocorrelation contrast ratio in the background-free case (3:1 before subtracting the background) and 670 fs full width at half maximum (FWHM) autocorrelation
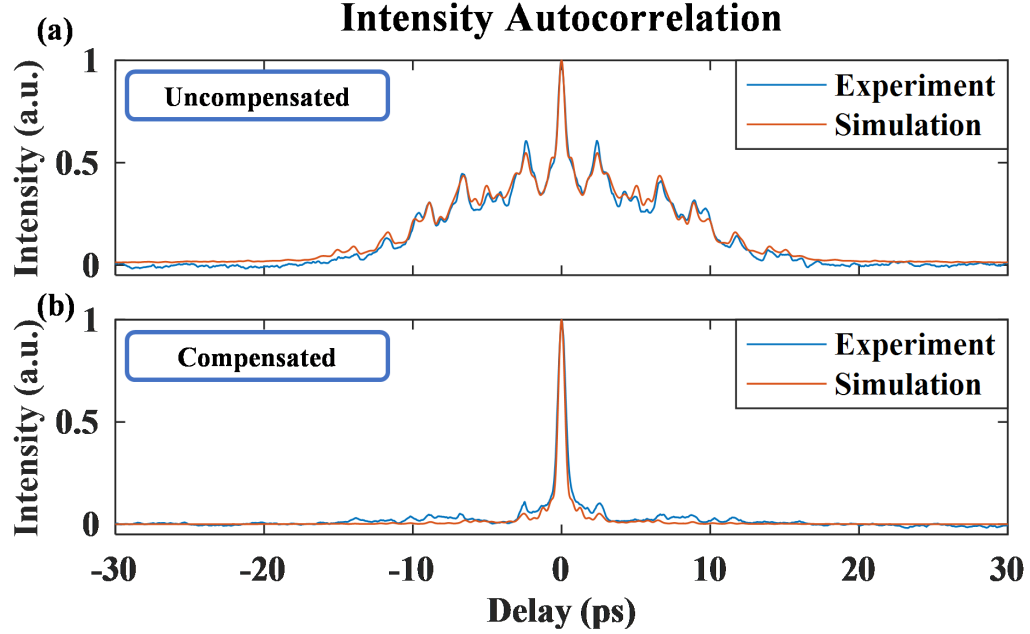
Fig. 2.5: Experimental and simulation results for MMF output optical field characterization and pulse compensation. (a) Intensity autocorrelation trace of MMF output field (MMF impulse response) in experiment (blue) and in simulation (red). (b) Intensity autocorrelation of compensated pulse in experiment (blue) and in simulation (red). Simulation results are calculated based on the measured power spectrum and characterized phase response.

width. The peak SHG signal after pulse compression is increased by about an order of magnitude compared to the SHG signal of the noise-like output field.

2.4 Spatial and Temporal Focusing at Two Output Locations

In a MMF with strong modal dispersion effects, the temporal and frequency speckles are expected to decorrelate rapidly in the spatial coordinate. We tested this expectation by using a standard SMF mounted on a translation stage to sample the field at two locations on the output surface of the MMF separated by 10 μm, as shown in Fig. 2.6. The MMF channel responses at the two output spots are plotted in Fig. 2.7 in both frequency and time domains. The autocorrelation data in Fig. 2.5 corresponds to output 1 in Fig. 2.7. The output field at any specific spatial spot acquires ran-
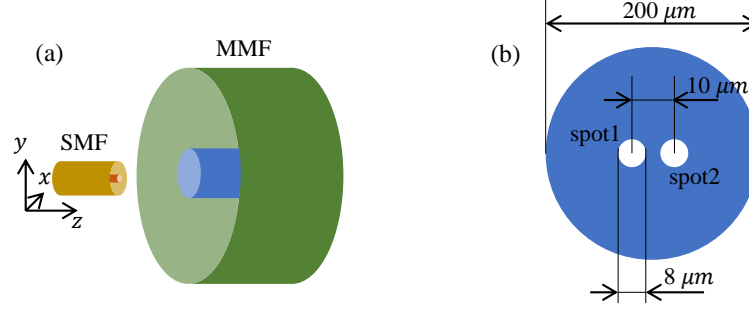
Fig. 2.6: Schematic diagrams for (a) MMF output sampling and (b) 2 output spots characterization and compensation

dom substructures in both time (temporal speckle) and frequency (spectral speckle). The temporal and spectral profiles are of course related by the Fourier transform. Comparison of the temporal and spectral profiles at the two output locations show a similar character but quite distinct details, confirming the expected decorrelation. The channel impulse responses shown in Figs. 2.7(c) and 2.7(d) are calculated from the power spectra measured by an optical spectrum analyzer (OSA) and the phase responses characterized via pulse shaping. As can be seen, multiple copies of transmitted pulses are received, with random attenuation (amplitude), delays and phases. A time delay spread of 10 ps can be observed at both output locations, but with different substructures. These data resolve the temporal speckles, which are averaged out in the photodetector measurements of Fig. 2.1(b). The multiple deep fades in the power spectra of Figs. 2.7(a) and 2.7(b) are a manifestation of the speckle in frequency and are in analogy with the deep fades that occur in strongly multipath RF channels [1, 44].

The decorrelation of the MMF channels at different output locations is further proven by focusing a transform-limited ultrafast pulse in space and time. As seen in Figs. 2.8(a)-2.8(d), when the pulse shaper is programmed to compensate the channel response corresponding to output 1, a strong peak will appear on the intensity autocorrelation trace measured at output 1, whereas the intensity autocorrelation measured at output 2 indicates a noise-like field. Conversely, when the pulse shaper
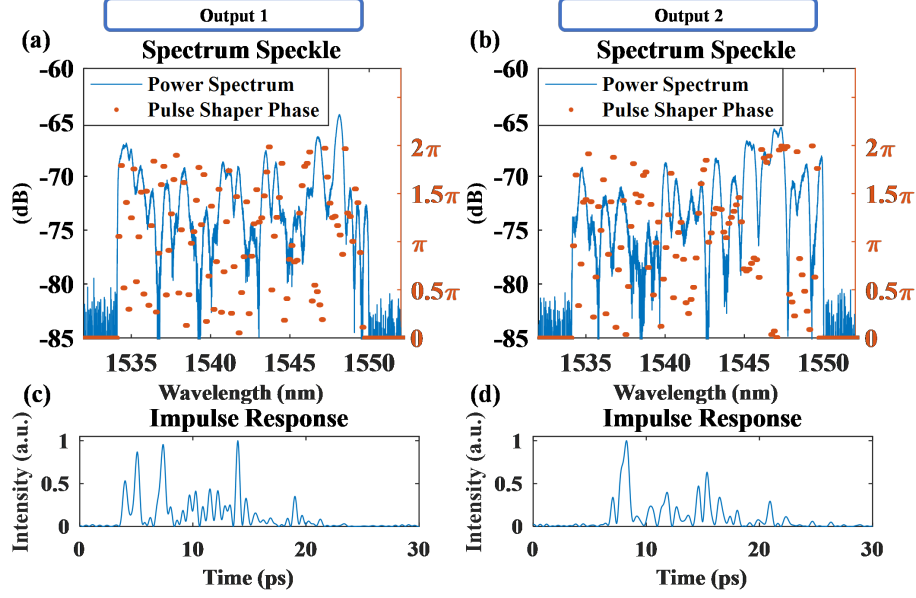
Fig. 2.7: Spectral speckles and temporal speckles at two different output locations separated by 10 μm. (a) and (b) Spectral speckles at output location 1 and at output location 2 power spectra (blue solid) are measured using optical spectrum analyzer (OSA) and phases (red dot) programmed on the pulse shaper are used to compensate the output fields. (c) and (d) Temporal speckles at output location 1 and at output location 2 the impulse responses are calculated from the frequency responses shown in (a) and (b) by inverse Fourier transform.

is configured to compensate the channel corresponding to output 2, the field at output 1 remains noise-like, with compression observed at output 2. Note that the peak values of the solid traces in Figs. 2.8(b,c) are normalized to the peak values of the traces in Figs. 2.8(a,d), respectively. The dotted traces in Figs. 2.8(b,c) are zoomed-in in the vertical scale to better display the 2:1 peak to envelope contrast of the noise-like fields. The spatially selective peaking in a specific input-output channel demonstrates space-time focusing of the MMF system. In this case, the transmitted information can be encoded for compression at a specific output spot, while the peak intensity remains low and potentially more difficult to detect at other output locations. This capability may bring opportunities for covert sharing of a MMF for multiple communications channels. To summarize, we have demonstrated space-time focusing of broadband ultrafast pulses distorted by modal dispersion in a multimode fiber. Our
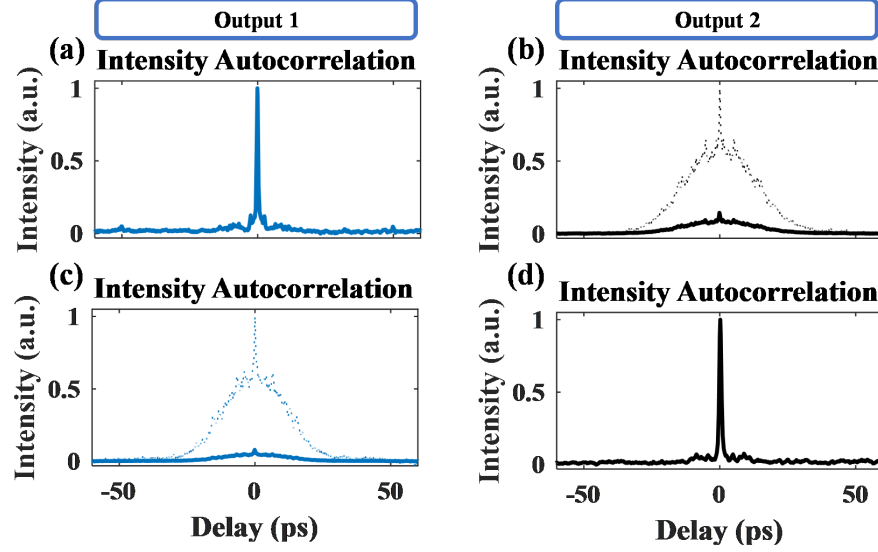
Fig. 2.8: Spatial and temporal focusing at MMF output surface using spectral phase compensation. (a) and (b) The optical field at output 1 is compensated the field at output 1 is a transform limited pulse whereas the field at output 2 remains noise-like. The solid trace in (b) is normalized to the peak value in (a). (c) and (d) The optical field at output 2 is compensated the field at output 2 is a transform limited pulse whereas the field at output 1 remains noise-like. The solid trace in (c) is normalized to the peak value in (d). The dotted lines in (b) and (c) are zoomed vertically.

approach uses phase compensation in the spectral domain (pulse shaping) and does not require interference with a reference field. Furthermore, although the current report employs a commercial pulse shaper constructed from discrete components, pulse shapers can also be realized on chip [90–92], opening possibilities for highly compact shaper-MMF modules. In contrast, wavefront shaping techniques rely on spatial light modulators, which are inherently free-space components. This work could contribute to new opportunities for nonlinear microscopy and imaging or space-division multiplexed optical communications through multimode fiber.

3. DYNAMIC WIRELESS MULTIPATH CHANNEL SOUNDING AND COMPENSATION

3.1 Multipath RF Wireless Channel Sounding and Compensation

As briefly introduced in Section 1.2, multipath is a propagation phenomenon in which the transmitted signals reach the receiver via different paths and interactions in a complex surrounding such as indoor, urban, or other cluttered environments. Characterizing the propagation of a static ultrawideband (UWB) RF multipath channel (channel sounding) has been largely studied in our group's previous experiments. The channel impulse response in the time domain is denoted by $h(t)$ and the channel frequency response $H(f)$ can be defined as following

$$H(f) = \mathcal{F}\{h(t)\} = |H(f)|e^{j\phi(f)} \tag{3.1}$$

Figure 3.1 shows a schematic diagram of the channel sounding process for finding $h(t)$. A spread spectrum linear chirp waveform, shown in Fig. 3.2(a) as an example, is generated by the electronic arbitrary waveform generator (AWG) and is broadcasted by the transmitter (Tx). At the same time, the received signal is recorded at receiver (Rx), shown in Fig. 3.2(b). Next, the channel response $h(t)$ and $H(f)$ can be calculated by deconvolution. Figure 3.2(c) and Fig. 3.2(d) is an example pair of $h(t)$ and $H(f)$. The delay spread in $h(t)$ and the numerous deep fades in $H(f)$ indicate strong multipath effects.

Time reversal (TR) and phase compensation (PC) are two examples of broadband RF channel compensation techniques. For TR, the precompensation waveform $v_{inTR}(t)$ fed to Tx is the time reversed channel impulse response. Mathematically, its Fourier transform is $H^*(f)$.

$$v_{inTR}(t) = h(-t) \tag{3.2}$$

$$V_{inTR}(f) = \mathcal{F}\{v_{inTR}(t)\} = \mathcal{F}\{h(-t)\} = H^*(f) \qquad (3.3)$$

The received signal at Rx (Fig. 3.3(b) in red solid) is the convolution of the transmitted waveform with the channel impulse response. And in the frequency domain, it is the magnitude squared of the channel's frequency response.

$$V_{outTR}(f) = \mathcal{F}\{v_{inTR}(t) * h(t)\} = \mathcal{F}\{h(-t) * h(t)\} = H(f)H^*(f) = |H(f)|^2 \quad (3.4)$$

It can be viewed as a pre-matched-filter [40], focusing the power of different frequencies into a specific time. This gives the maximum peak voltage with fixed transmitted power because the spectral phase of the received signal is compensated signal in the
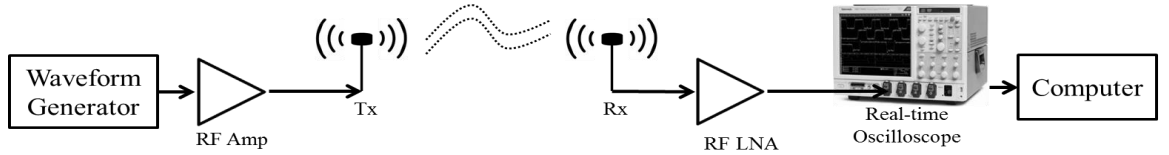
Fig. 3.1: Experimental setup of broadband channel sounding. Amp, amplifier; LNA, low noise amplifier; Tx, transmitter; Rx, receiver.
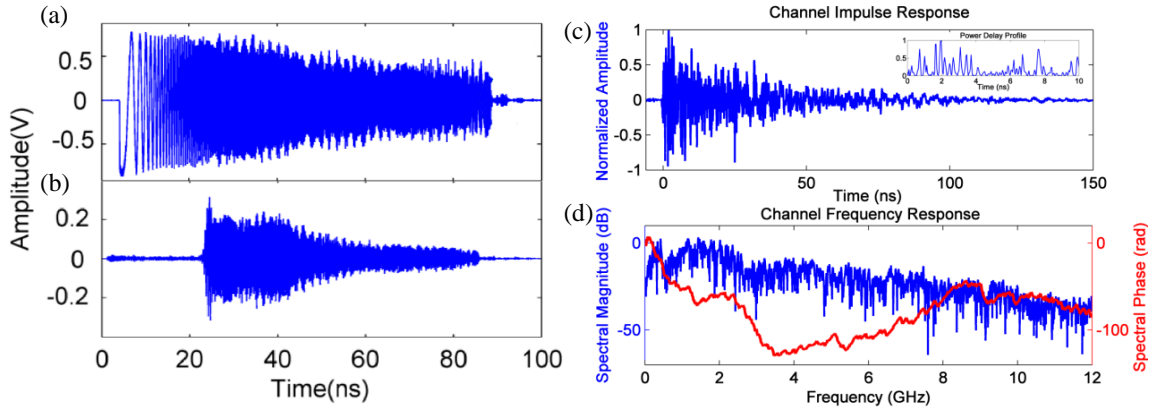
Fig. 3.2: Spread spectrum channel sounding, adapted from [45], and channel response, adapted from [93]. (a) Broadband linear chirp signal sent to Tx. (b) Received waveform at Rx. (c) Impulse response of a non-line-of-sight (NLOS) indoor environment over 150 ns time window. Inset, zoom-in of power delay profile over 10 ns window. (d) RF power spectrum and unwrapped spectral phase of channel frequency response.
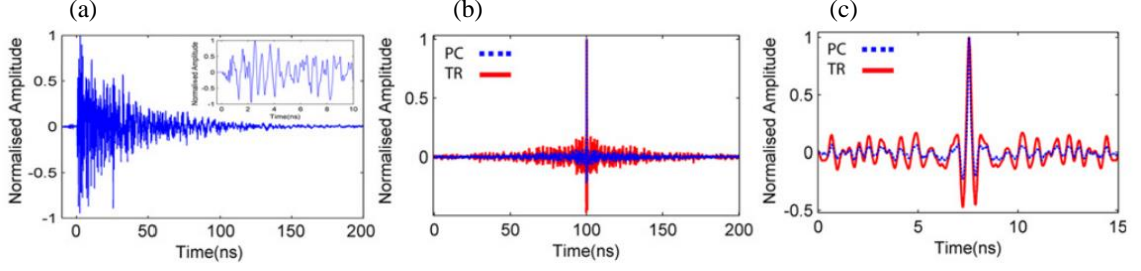
Fig. 3.3: PC and TR compensation results in NLOS environments, adapted from [40]. (a) Impulse response of NLOS omi-directional antennas over 200 ns time window. Inset: magnification of the first 10 ns of the impulse response. (b) Received responses from TR and PC channel compensation experiments over the channel presented in (a). (c) Zoom-in of the main peaks shown in (b).

frequency domain. However, the squaring of the spectral magnitude downgrades the side lobe suppression performance, especially compared to PC.

The principle of PC can be explained as compensating the spectral phase of the impulse response without squaring the magnitude. The pre-distorted waveform v_{inPC} is generated by conjugating the spectral phase $\phi(f)$ with the inverse Fourier transform.

$$V_{inPC}(f) = \mathcal{F}\{v_{inPC}(t)\} = e^{-j\phi(f)} \tag{3.5}$$

Therefore, the spectrum of the final compensated signal can be expressed as Eq. 3.6, again with zero spectral phase.

$$V_{outPC}(f) = V_{inPC}(f)H(f) = e^{-j\phi(f)}|H(f)|e^{j\phi(f)} = |H(f)| \tag{3.6}$$

Example results for TR and PC compensation are shown in Fig. 3.3

3.2 Dynamic Channel and Processing Architecture

Rapid updating of the channel information and the precompensation waveform design will be essential in the case of mobile communications. In this work, we
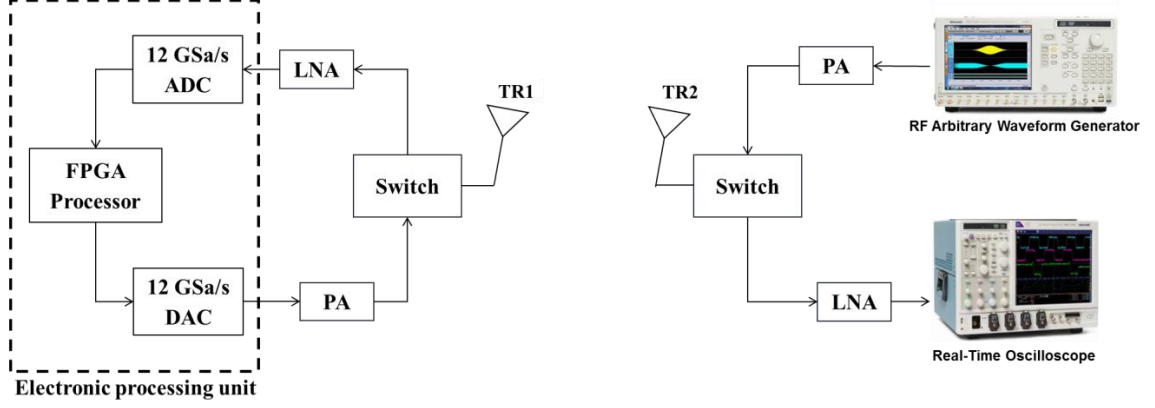
Fig. 3.4: Experimental setup for ultrabroadband dynamic channel sounding and multipath precompensation with rapid update. TR, transmitter-receiver module; PA, power amplifier; LNA, low noise amplifier.

demonstrate sounding and precompensation of UWB multipath channels on a time scale suitable for mobile operation. First of all, a brief estimation of the required updating speed for sounding and precompensation is needed. Imagine a receiver antenna moving at 36 km/h, much faster than we are likely to encounter at least in a typical indoor environment. With highest frequency of 10 GHz (3 cm wavelength), the decorrelation of the channel should become significant a wavelength away (3 cm). Therefore, it is required to update the channel information and the precompensation waveform for every 1 cm of displacement. This means the update speed is not slower than 1 ms, far beyond the processing speed of the conventional equipments used in the previous section's static channel techniques. In order to achieve rapid update to keep peaking and signal-to-noise/interference enhancement at the receiver, a commercially available module (Curtiss-Wright CHAMP-WB-DRFM) comprising of high-speed analog-to-digital conversion (ADC), digital-to-analog conversion (DAC), and FPGA (Xilinx Virtex 7) units that are tightly coupled is exploited to break communications bottlenecks.

Figure 3.4 shows the experimental configuration. Different from our previous setup shown in Fig. 3.1, here we use transmit-receive (TR) modules with fast time switching for bidirectional transmission. The whole TR1 block is placed on a moving cart for

mobile communication while the location of TR2 block is fixed. TR1 and TR2 are set for non-line-of-sight (NLOS) configuration for a more field-use case with densely multipath. First, TR2 is set to broadcast spread spectrum chirp signal generated by RF-AWG and TR1 starts as a receiver. Once TR1 receives a signal past the pre-set power threshold, the sounding process is initiated and executed for channel response calculation by the processing unit. The transmitted chirp waveform is pre-stored in the memory of processing unit. Next, the precompensation waveform is calculated and generated by DAC. A control signal is also processed by the processing unit and sent to the RF switch in order to set TR1 as a transmitter to transmit the precompensation waveform. After transmitting, TR1 is switched back to receiving mode by a control signal from DAC. Meanwhile, TR2 is turned into a receiver soon after transmitting the chirp waveform for sounding and waits to receive the compensated peak signal. The RF switch at TR2 is controlled by a signal with 40 μs time period, which means that the communication speed is at least 25 thousand symbols per second.

The overall architecture of FPGA-based sounding and compensation for dynamic ultrabroadband RF wireless channels is shown in Fig. 3.5, and the processing time for each step is shown in Table 3.1. The hardware implemented in the FPGA is designed using SystemVerilog (a hardware description language) and the development environment was provided by Curtiss-Wright and Xilinx. The timing and the data flow of the algorithm are explained in the following, with reference both to the Curtiss-Wright electronics processing unit and to the external equipment (RF-AWG and real-time oscilloscope):

Channel sounding.

Time domain switches are set to allow transmission from RF-AWG to electronics processing unit. This portion of the operation takes place during $\sim 6 \ \mu s$.

- The ADC is used to capture an incoming signal for the channel sounding operation. The incoming signal is the sounding waveform generated the RF-AWG and

distorted by transmission through the multipath channel. Generally the sounding waveform generated by the RF-AWG is chosen to be a 6 GHz bandwidth, 80 ns linear up-chirp. During the sounding process, the up-chirp waveform is retransmitted every 170.67 ns (2048 time samples) for a total of 16 transmissions.

- The ADC controller receives the data sampled by the ADC. Given that the clock of the FPGA is 375 MHz, 32 samples are loaded into the ADC controller in each clock period to achieve 12 giga samples per second (GS/S)

- The averager block averages together successive length-2048 vectors (corresponds to successive 170.67 ns periods of the repeated sounding waveform) captured by the ADC. The intent is to suppress noise and interference both for purposes of recognizing when a sounding signal is present and then to extract the channel response.

- When the averaged received signal achieves a specific value, the Threshold Detection block recognizes that a sounding signal is present. The averaged received signal is then presented to the FFT block.

- The FFT block is implemented using an IPCore provided by Xilinx Vivado. This block is configured to process the forward Fast Fourier Transform in a high throughput mode. The input of this block is the filtered and averaged received signal comprising a length-2048 vector. The output contains 2048 complex values corresponding to the frequency spectrum of the received signal.

- The inverse of the complex spectrum of the transmitted sounding waveform (the chirp signal), denoted $1/X(\omega)$, is calculated in advance offline and is stored in a memory based on look-up tables (LUTs).

- A complex multiplier block multiplies the complex frequency spectrum of the received signal with $1/X(\omega)$ retrieved from memory. The result of this mul-
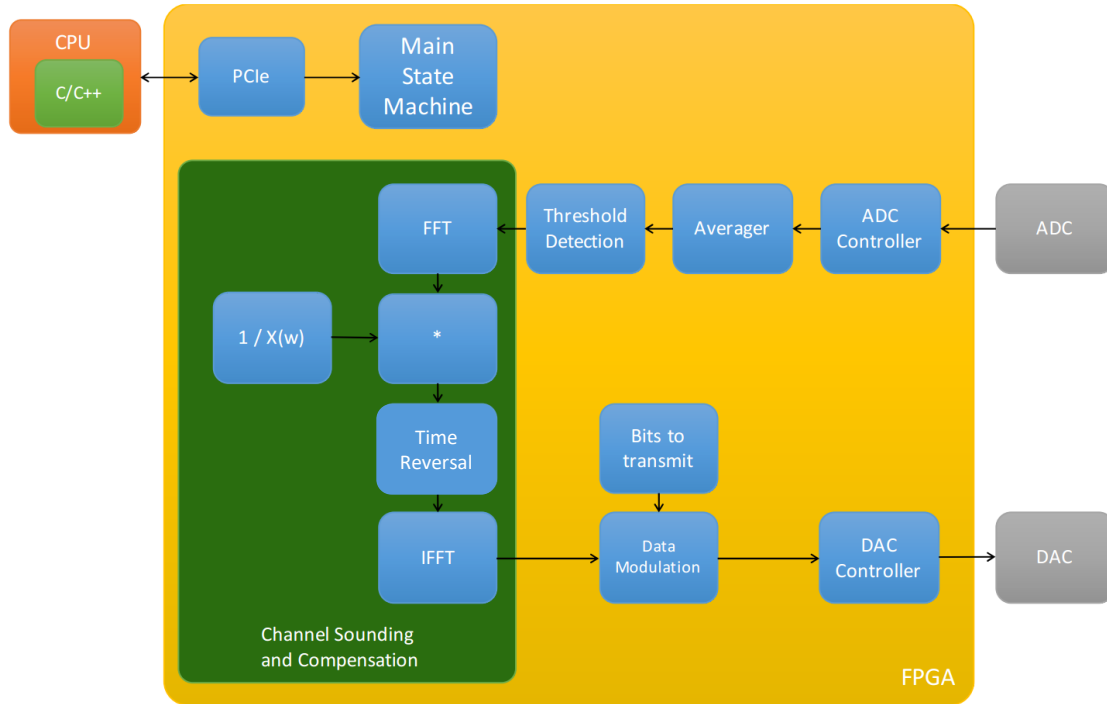
Fig. 3.5: Block diagram of processing architecture realized in the FPGA for channel sounding and compensation.

tiplication corresponds to the channel frequency response and completes the channel sounding part of the cycle.

Channel compensation

Time domain RF switches are now set to allow transmission from the electronics processing unit (TR1) to the real-time scope (TR2). For the following discussion in this section we assume time reversal is used. A similar flow can apply phase compensation with only minor modifications. This portion of the operation takes place over $\sim 34\ \mu s$.

- For channel compensation, the time reversal process is implemented by changing the sign of the imaginary part of each complex value in the channel frequency response.

- The output of the time reversal block $H^*(f)$ is sent to the FFT block, which is configured to perform the inverse fast Fourier transform. The output of this process is called the phase precompensated signal ($v_{inPC}(t)$ in Eq. 3.5).

- The DAC controller receives the digital representation of the precompensated signal $h(-t)$ and sends it to the DAC, which finally generates the analog signal that can be amplified and then applied to the antenna to carry out the bidirectional, precompensated transmission.

The total processing time is $\sim 30\mu s$ as shown in Table 3.1. An additional 10 μs time budget is allowed here as the time period for each handshaking is set to be 40 μs. This is 25 times faster than 1 ms updating time estimated at the beginning of this section.

Table 3.1: Processing Time

Block	Processing time
Data transfer between FPGA and ADC/DAC	47 ns
Threshold detection	5.33 ns
Averager	5.33 ns
FFT (2048 vector)	18 μs
Multiplication	16 ns
IFFT (2048 vector)	11.5 μs
Total channel sounding and compensation	**29.6** μs

3.3   Time-Domain Reciprocity Verification

As can be seen from section 3.2, this system is designed under the assumption of reciprocity between the two transceiver antennas. Therefore, the rest results of the reciprocity for this bidirectional experimental scheme are discussed in this section. The reciprocity test measurements use the AWG and realtime oscilloscope for waveform generation and recording, together with the components (time domain RF switches, amplifiers, antennas) purchased for the testbed. The high speed FPGA
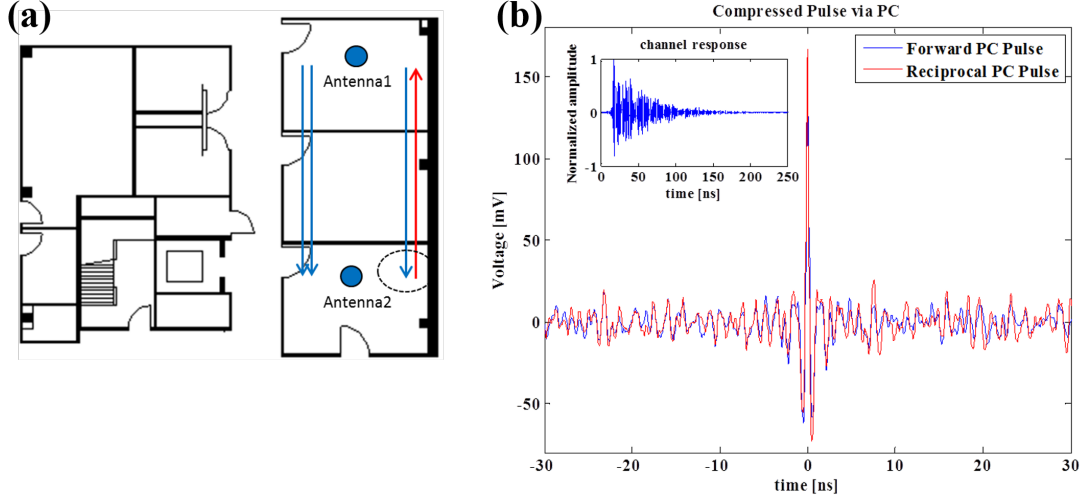
Fig. 3.6: Time-domain reciprocity test. (a) Environmental layout and position of the two antennas. (b) Time-domain waveforms measured in forward and backward propagation directions (relative to the direction in which channel sounding was performed). The forward (blue) and backward (red) waveforms are very close, confirming time-domain reciprocity. Inset: channel response without compensation.

processing unit is not available at this point. Two channel compensation experiments are performed with two transceiver antennas placed at two rooms separated by two walls (10 m separation), as shown in Fig. 3.6(a). Channel sounding is only performed once, with AWG connected to antenna 1 as the transmitter and the received waveforms is received by antenna 2, recorded by the realtime scope. The information from channel sounding received waveforms is used to process the channel response. The multipath response has total time duration around 80 ns, as shown by the inset of Fig. 3.6(b). For channel compensation, the AWG is programmed for spectral phase compensation. It is first performed in the forward direction; the compensation waveform is applied to and broadcast by antenna 1 and received by antenna 2, the same direction as the channel sounding operation. Next, channel compensation is performed in a backwards and reciprocal direction; the entire multipath environment stays the same except the positions of the AWG and the realtime scope are switched, so that the compensation waveform is applied to and broadcast by antenna 2 and

received at antenna 1. In both cases, a strong highly compressed peaking signal is received at the receiver antenna. The actual waveforms are nearly identical in both forward and backward transmission cases, confirming the time domain reciprocity.

3.4 Static Channel Sounding and Compensation with FPGA-based Processing Unit

After setting up the FPGA-based processing unit, we first perform channel sounding and compensation using the static approach. Here, both transceiver antennas are held at fixed locations resulting in a time-invariant propagation channel. The linear chirpped sounding waveforms are generated by the AWG and broadcast by antenna 1. The signal received at antenna 2 is digitized by the ADC; the channel response is extracted by Fourier transform processing and deconvolution algorithms calculated offline; and the precompensation waveform is generated using DAC, amplified, and applied to antenna 2. The peaking waveform received back at antenna 1 is recorded by the realtime scope. For these tests, the two antennas are about 5 meters apart and separated by one wall. Both time reversal and phase compensation precompensation algorithms are applied here. Channel sounding and compensation results are shown in Fig. 3.7. Figure 3.7(a) shows the calculated time domain channel impulse response. Fgiure 3.7(b) and Figure 3.7(c) show the waveforms received with precompensation for time reversal and phase compensation, respectively. In both cases sharp, narrow peaks are obtained. The peaks repeat periodically because the precompensation waveform is generated and broadcast periodically, repeating at 6 MHz rate. The peaks have higher amplitude for time reversal (matched filter), but the peak to average power ratio and sidelobe suppression are better for phase compensation – both of which are expected. These results verify successful operation of the FPGA-based processing unit for channel sounding and precompensation under static channel conditions.
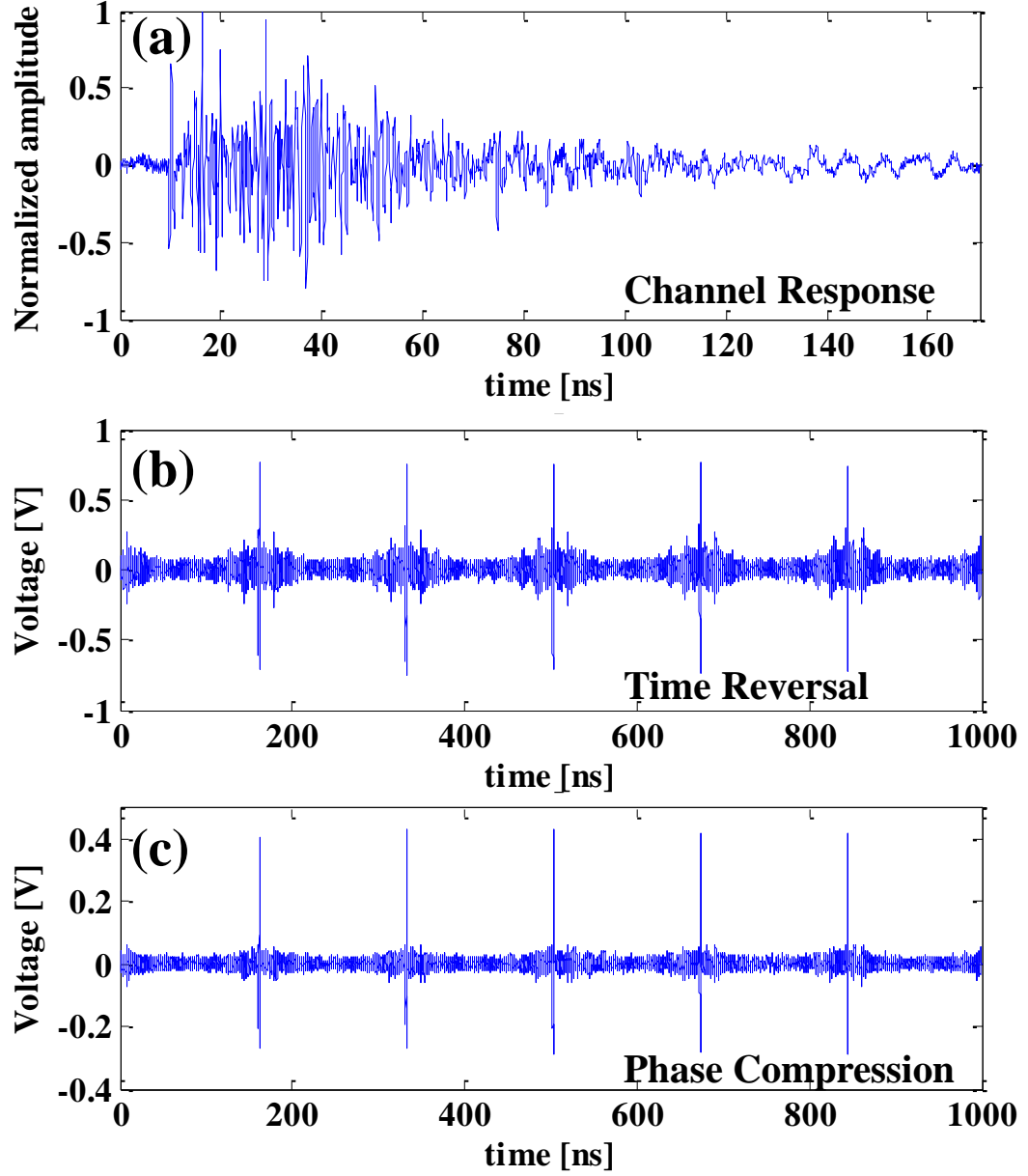
Fig. 3.7: (a) Channel sounding and compensation realized using FPGA-based processing unit. (a) Deconvolved channel response. (b,c) Compensation achieved under (b) time reversal and (c) spectral phase compensation.

3.5 Dynamic Channel Compensation

A demonstration of dynamic channel compensation is performed. During the experiment, it is possible to maintain compensation with peaking at the receiver

under dynamic conditions. The experiment runs in our laboratory room and the corridor. TR2, the stationary antenna connected with RF AWG and oscilloscope, is kept in a lab room while TR1 and the whole FPGA processing unit is placed on a cart moving along the corridor. Antennas positions with floor plan are shown in Fig. 3.8. The total motion distance of the cart is about 10 meters and the moving speed of the cart is around 1.2 km/h (0.33 m/sec). Two sets of selected data are plotted in Fig. 3.8, one with real-time updating channel information (center column in Fig. 3.8) and the other one with fix channel information (left column in Fig. 3.8) of only one specific TR1-TR2 link just for comparison. From the result, the system is able to maintain a strong time reversal peak over the full range of motion examined. In contrast, when the channel response was only measured for one position and keeping this compensation waveform, a time reversal peak can only be observed when the cart is very close to the position where sounding is performed, meanwhile stating the localization property of a complexed multipath RF channel.

In summary, we implement the UWB multipath wireless channel sounding and compensation on a dynamic channel. With the help of a FPGA processing unit, we demonstrate an updating rate up to 25 KHz. To the best of our knowledge, no experiment of this type have been previously reported.
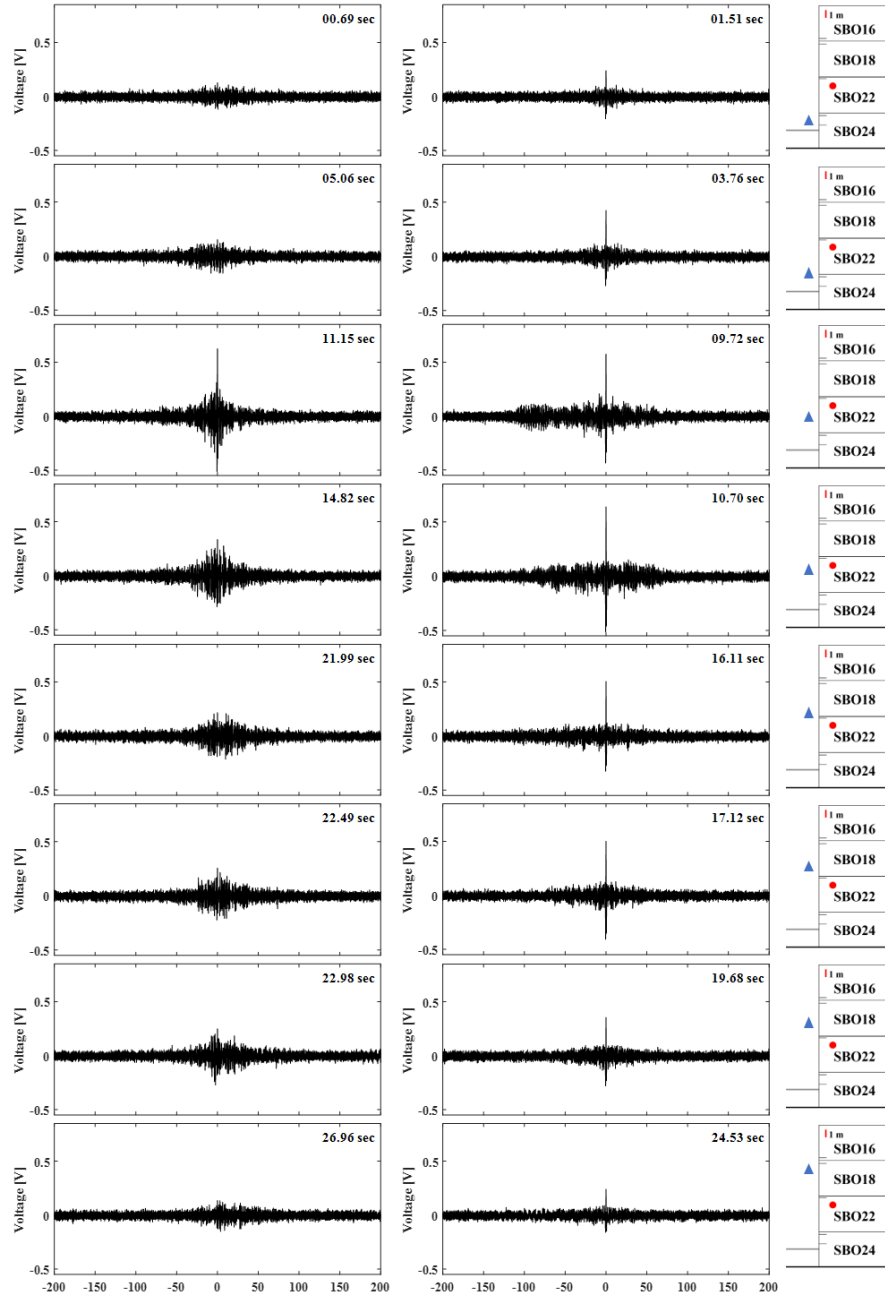
Fig. 3.8: Waveform recorded at receiver end with unchanged compensation waveform (left column) and real-time updated compensation waveform (center column). Right column, floor plan; Blue triangle dot, moving antenna (TR1); Red circle dot, static antenna (TR2)

4. ULTRABROAD BAND PHOTONIC PHASE SHIFTER FOR W-BAND MONOPULSE RADAR BEAMFORMING

4.1 Photonic-Assisted Arbitrary Waveform Generation

As previously discussed in section 1.3, photonic-assisted RF-AWG techniques based on Fourier transform optical pulse shaping [38] and frequency-to-time mapping (FTM) are exceptionally powerful and provide more competitive performance in terms of generated signal complexity (extremely high bandwidth) and stability (low phase noise). Figure 4.1 shows a simplified experimental layout of photonic-assisted RF-AWG, and a schematic diagram visualizing the generic implementation of FTM. The spectrum broadband optical short pulse is first tailored to the targeting shape via the pulse shaping technique. After being stretched in time by first order dispersion (quadratic spectral phase, resulting in linear frequency dependent delay) when propagating along the dispersive element (normally single mode fiber or dispersion compensating fiber), the short pulse in the time domain will be a scaled replica of

Portions of the results in this chapter have been published in Refs. [94].
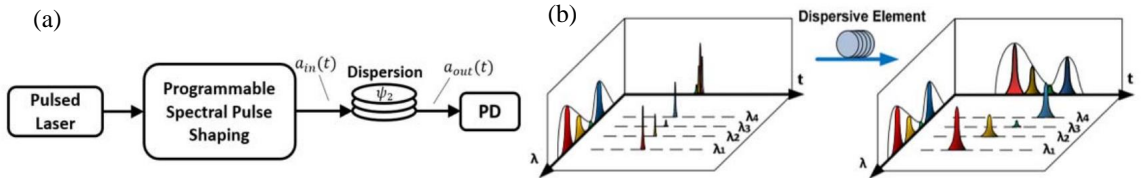
Fig. 4.1: RF-AWG based on optical spectral pulse shaping and frequency-to-time mapping (FTM), adapted from [3]. (a) Schematic diagram of the generic setup. (b) Illustration of frequency-to-time mapping in a dispersive element.
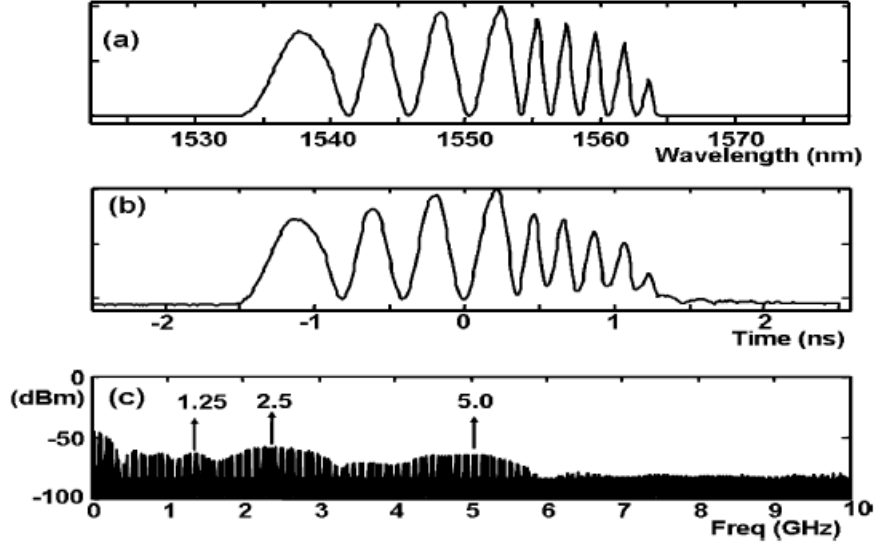
Fig. 4.2: FTM-based microwave arbitrary waveform generation using a reflective optical Fourier transform pulse shaper, adapted from [74]. (a) Filtered optical spectrum showing chirped modulation. (b) Measured time-domain RF waveform showing cycles at 1.25, 2.5, and 5 GHz with great resemblance with shaped optical spectrum in (a). (c) Corresponding broadband RF power spectrum.

the tailored power spectrum. Propagating an optical field $a_{in}(t)$ through a quadratic dispersive element with added spectral phase ψ_2 gives the output optical field $a_{out}(t)$

$$a_{out}(t) \propto e^{-j(\frac{t^2}{2\psi_2})} \int a_{in}(t') e^{-j(\frac{t'^2}{2\psi_2})} e^{-j(\frac{tt'}{\psi_2})} \, \mathrm{d}t' \qquad (4.1)$$

When dispersion ψ_2 is large enough compared to the time aperture of the input optical pulse. The $e^{-j(\frac{t'^2}{2\psi_2})}$ term inside the integral in Eq. 4.1 can be dropped, fulfilling the far-field condition. In this case, the remaining terms in the integral display a Fourier transformation. The intensity of the output optical signal can be written as

$$|a_{out}(t)|^2 \propto |A_{in}(\omega = -\frac{t}{\psi_2})|^2 \qquad (4.2)$$
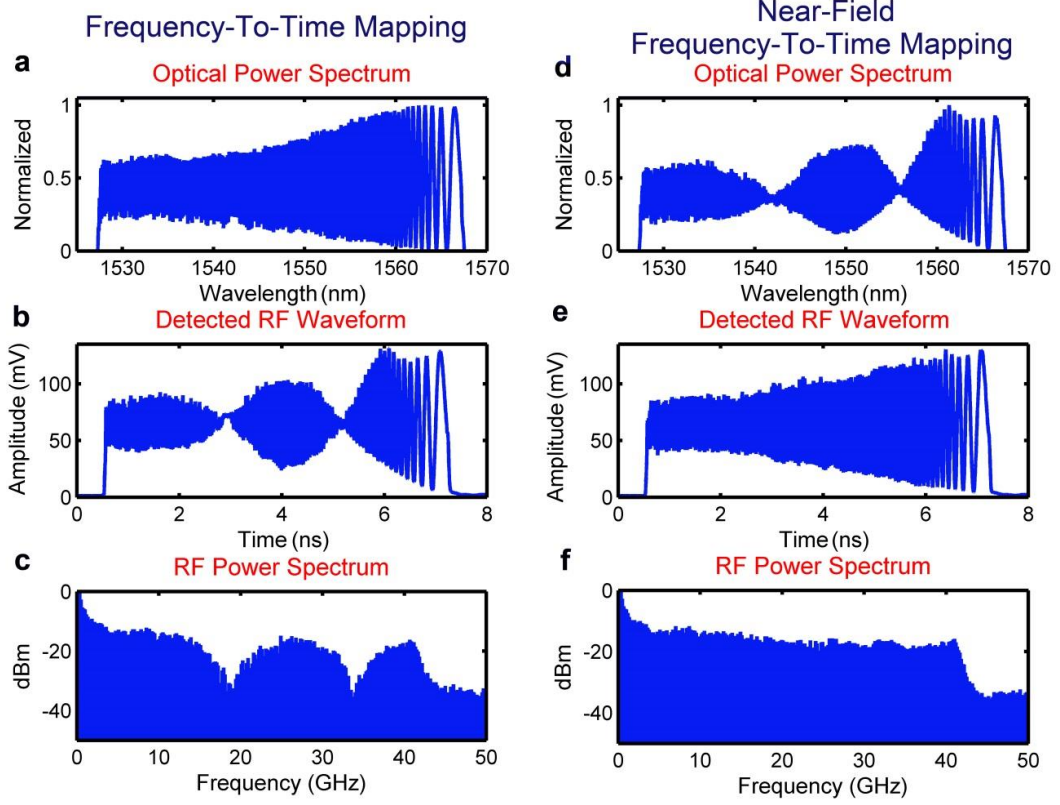
Fig. 4.3: Generating down-chirp RF waveform over frequencies from baseband to 41 GHz with time aperture of 6.8 ns, corresponding to a time-to-bandwidth product (TBP) of 280, adapted from [3]. (a-c) Waveforms from conventional frequency-to-time mapping. Generated RF waveform is badly distorted and certain frequencies are strongly attenuated. (d-f) Waveforms from near-field frequency-to-time mapping (NF-FTM). An undistorted chirp signal is obtained and the RF spectrum extends smoothly out to 41 GHz with less than 5 dB roll-off in respect to the 4 GHz frequency component.

The output optical intensity $|a_{out}(t)|^2$ can be converted to an RF waveform via photo-detection. An example of arbitrarily generated broadband RF waveform is shown in Fig. 4.2, acquired from our group's previous work [74]. However, when the far-field condition fails due to lack of dispersion amount, the generated RF waveform will suffer a significant distortion, shown in Fig. 4.3(b). Therefore, near-field frequency-to-time mapping (NF-FTM) approach is introduced in [3] to overcome the far-field limitation. In this case, the pulse shaper is programmed to yield a complex envelope

$$a_{NF-FTM}(t) = a_{FTM}(t)e^{j\frac{t^2}{2\psi_2}} \qquad (4.3)$$

As shown in Figure 4.3(e), an undistorted target broadband RF waveform is achieved via NF-FTM compared to the distorted case in Fig. 4.3(b) via conventional FTM. Detailed discussion can be found in [3] for near-field virtual time lens correction. Such approach provides the possibility of pushing the photonic-assisted AWG from conventional lower RF frequency band to higher frequency region such as W-band AWG.

4.2 Photonic Phase shifter Setup for W-band Monopulse-Like Radar Array

The W-band antenna array experimental setup, shown in Fig. 4.4, consists of three parts: photonic-assisted AWG, fast photo-detection, and wireless antenna channel. User defined optical profiles, which later through photodetection turn into desired W-band waveforms, are generated by the NF-FTM technique discussed in previous section. It has been shown that the W-band waveforms generated in this way show low phase noise and timing jitter [56]. In the experiment, the optical pulse from the laser source is stretched in time by the dispersive fiber, with 37.5 ps/nm total dispersion. After an input pulse passes through the dispersive fiber, it is splited into two arms by a fiber splitter and spectrally shaped by two pulse shapers. Therefore, the two optical waveforms in the time domain are the stretched replicas of the tailored power spectra. The two pulse shapers in our setup are programmed independently, each with 500 super-pixels, covering the entire optical C-band (5 THz bandwidth with 10 GHz spectral resolution). The optical signals from the photonic-assisted AWG are converted to millimeter-waves (MMWs) by two uni-traveling carrier photodiode (UTC-PD) based waveguide-coupled photomixers (one homemade [50], one commercial (NTT Electronics IOD-PMW-13001)). These two waveguide photomixers are connected to two horn antennas which are placed side-by-side, separated by $\sim$ 2 cm,
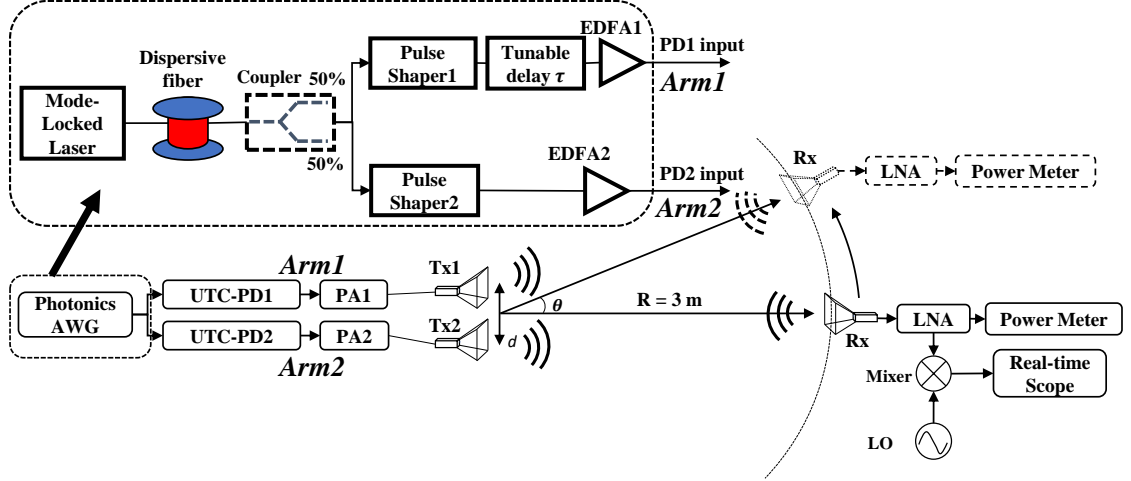
Fig. 4.4: Experimental arrangement of photonic phase shifter for monopulse radar. EDFA, erbium doped fiber amplifier; PD, photodiode; AWG, arbitrary waveform generation; UTC-PD, uni-traveling carrier photodiode based waveguide-coupled photomixer; PA, power amplifier; Tx, transmitter; Rx, receiver; LNA, low noise amplifier; LO, local oscillator; $d = 2$ cm, $R = 3$ m.

to serve as the transmitter array. A third horn antenna, which sits on a swing arm controlled by a programmable translation stage, located 3 meters away and facing the two transmitters, serves as the receiver. All three antennas are identical with the same 20 dB antenna gain across the full W-band.

To illustrate the photonic assisted AWG, we program the optical pulse shaper to generate a linearly chirped W-band waveform, covering 80 to 95 GHz with 1.5 ns time duration and 4 ns repetition period. For simplicity, only one transmitter is enabled for demonstarting W-band waveform generation. Figure 4.5(a) shows the down-converted signal at the receiver (Rx) antenna (with zero angular displacement), recorded by a real-time oscilloscope with a sampling rate of 50 GS/s. The mixer, with ~ 17 GHz intermediate frequency (IF) bandwidth, down-converts the received chirp signal to 2–17 GHz when the local oscillator (LO) frequency is set to 78 GHz. The reconstructed W-band waveform shown in Fig. 4.5(b) is calculated offline by directly
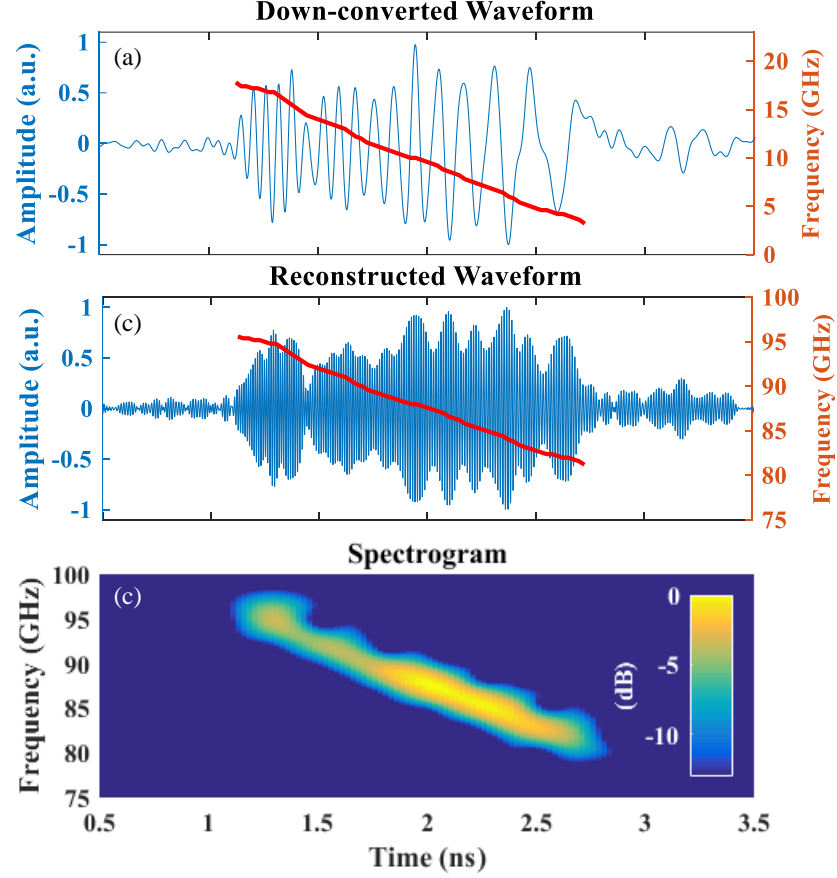
Fig. 4.5: Photonic-assisted AWG via NF-FTM in W-band. (a) W-band chirp signal from a single transmitter and its instantaneous center frequency, measured at the receiver end after down-conversion, showing 15 GHz bandwidth. Transmitted chirp, 80–95 GHz. LO frequency, 78 GHz. (b) Reconstructed received W-band chirp signal and its instantaneous center frequency. (c) Spectrogram of (b).

up-converting the spectrum of the waveform shown in Fig. 4.5(a) by the LO frequency and inverse Fourier transforming.

4.3 Sum and Difference Interference in Broadband W-band Monopulse Chirped Radar

We now demonstrate operation of the 2-element antenna transmitter array. In-phase and out-of-phase interference is first investigated in the time domain. The two pulse shapers are programmed to generate the W-band waveforms described in
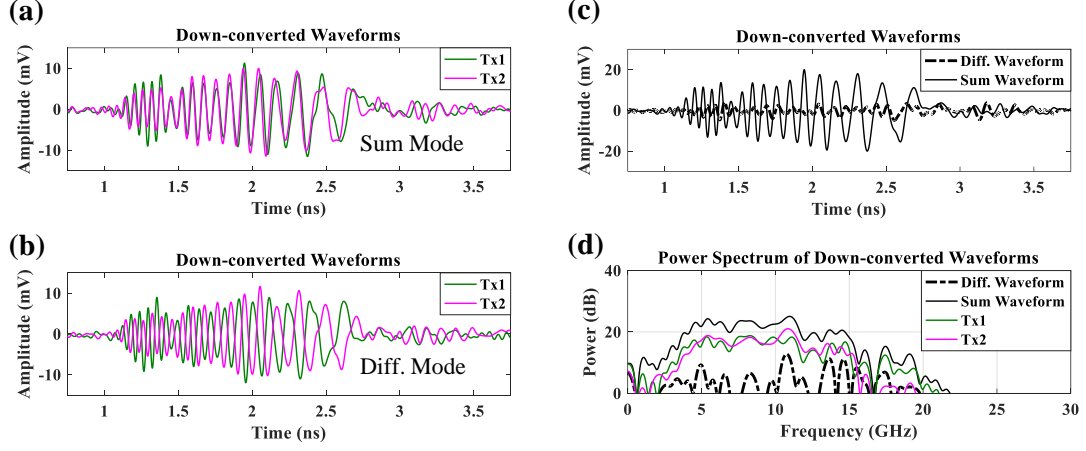
Fig. 4.6: Far-field antenna array measurement in the time domain. (a) Down-converted waveform at Rx when Tx1 on Tx2 off (green), Tx1 off Tx2 on (purple). Feeding waveforms for Tx1 and Tx2 are in phase. (b) Similar to (a) but feeding waveform for Tx1 and Tx2 are out of phase. (c) Down-converted sum (black solid) and difference (black dash) interference waveforms at Rx when both Tx are switched on. (d) Spectrum analysis of received signal. Black solid, Tx1 and Tx2 are in phase and both switched on. Black dash, Tx1 and Tx2 are out of phase and both switched on. Green solid, Tx1 on and Tx2 off. Purple solid, Tx1 off and Tx2 on.

the last section, but with either the same or opposite polarities. The transmitted waveforms are measured one at a time at the receiving antenna, which is set to the center of the transmitter axis with angular offset $\theta = 0°$, as shown in Fig. 4.4. The down-converted RF waveforms are shown in Fig. 4.6(a) for the same polarity and in Fig. 4.6(b) for the opposite polarity. The ability to impose a uniform π phase shift (polarity change) across the entire 15 GHz bandwidth is clearly visible. Figure 4.6(c) shows the down-converted received waveforms with both transmitters operating simultaneously. For the same polarity case (black solid), constructive interference of the two transmit signals across the entire waveform is observed; for the opposite polarity case (black dash), destructive interference occurs. The destructive interference trace shows minimum amplitude over the entire time aperture, while the amplitude of the constructive interference trace doubles that of the single-transmitter case. In addition, the RF power spectra over the down-converted frequency band are obtained via offline computation and displayed in Fig. 4.6(d). The average extinction ratio
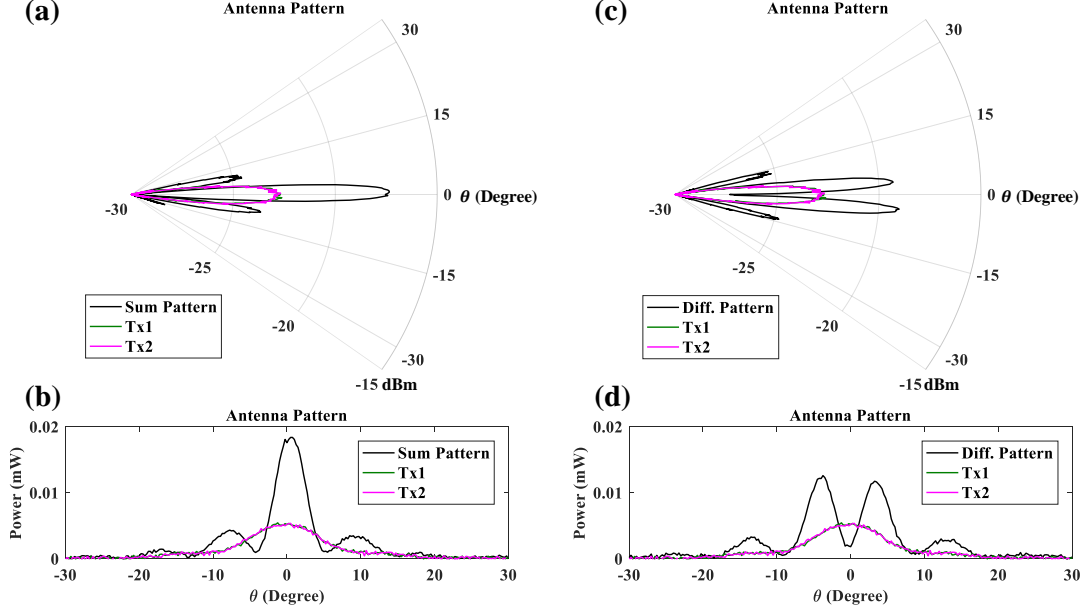
Fig. 4.7: Far-field antenna pattern measurement. (a,b) Far-field (3 m) broadband antenna array pattern with Tx1 and Tx2 in phase. Polar plot with log scale in (a) and Cartesian plot with linear scale in (b). (c,d) Far-field (3 m) broadband antenna array pattern with Tx1 and Tx2 out of phase. Polar plot with log scale in (c) and Cartesian plot with linear scale in (d). The measured powers at $\theta = 0°$ are 22.1 μW and 0.65 μW for in-phase and out-of-phase transmission, respectively; the power at $\theta = 0°$ with only a single transmitter enabled is 5.81 μW.

over 2-17 GHz (corresponding to 80-95 GHz in the W-band) between the in-phase (black solid) and the out-of-phase (black dash) is 15.96 dB. Moreover, the amplitude doubling shown in Fig. 4.6(c) in solid black appears in Fig. 4.6(d) in the form of 6 dB gain between the in-phase interference (black solid) and the single-Tx (green solid and purple solid) power spectra.

To illustrate spatial manipulation of the far-field antenna pattern, the previously described chirps are measured at the receiver using a W-band power meter, which gives the W-band power integrated over frequency (time). The far-field pattern is acquired by step-wise sweeping the receiver antenna over an arc, from $\theta = -30°$ to $+30°$ with a 0.25° angular increment. The measurement is conducted in both the sum and difference scenarios. The obtained results are plotted in Figs. 4.7. In the sum

interference case, both the polar (Fig. 4.7(a)) and Cartesian (Fig. 4.7(b)) plots show a constructive peak at the center. On the contrary, when the transmitters broadcast chirps with the opposite polarity, a null is observed at $\theta = 0°$, shown in Fig. 4.7(c) and (d). An extinction ratio of 15.31 dB between the sum and difference patterns at $\theta = 0°$ is observed, in excellent agreement with the extinction ratio estimated from the time domain data (Fig. 4.6).

In summary, we use photonic-assisted arbitrary waveform generation and waveguide-coupled UTC photomixers to drive a two-element antenna array with 15 GHz chirp waveforms in the W-band frequency region. By changing the relative polarity of the drive waveforms, we have achieved constructive and destructive interference of the on-axis radiation with 15 dB average contrast over 80-95 GHz. Far-field antenna array patterns are also acquired, proving the capability of focusing energy in different spatial directions by changing the phase between two broadband transmit waveforms.

4.4   Off-Axis Time Domain Waveforms

Furthermore, time domain waveform measurement is performed, especially when two receivers are placed symmetrically to the center axis (Tx array boresight). The absolute value of the Rx angular displacement can be obtained through both sum and difference received waveforms. However, only difference received waveform contains the opposite phase feature when Rx positions are symmetric to the transmitter center axis.

The W-band linear chirped waveform can be written as $C(t)$. When sum pattern are transmitted, we have two antenna broadcast waveform with same polarity.

$$Tx1_{sum}(t) = C(t) \tag{4.4a}$$

$$Tx2_{sum}(t) = C(t) \tag{4.4b}$$
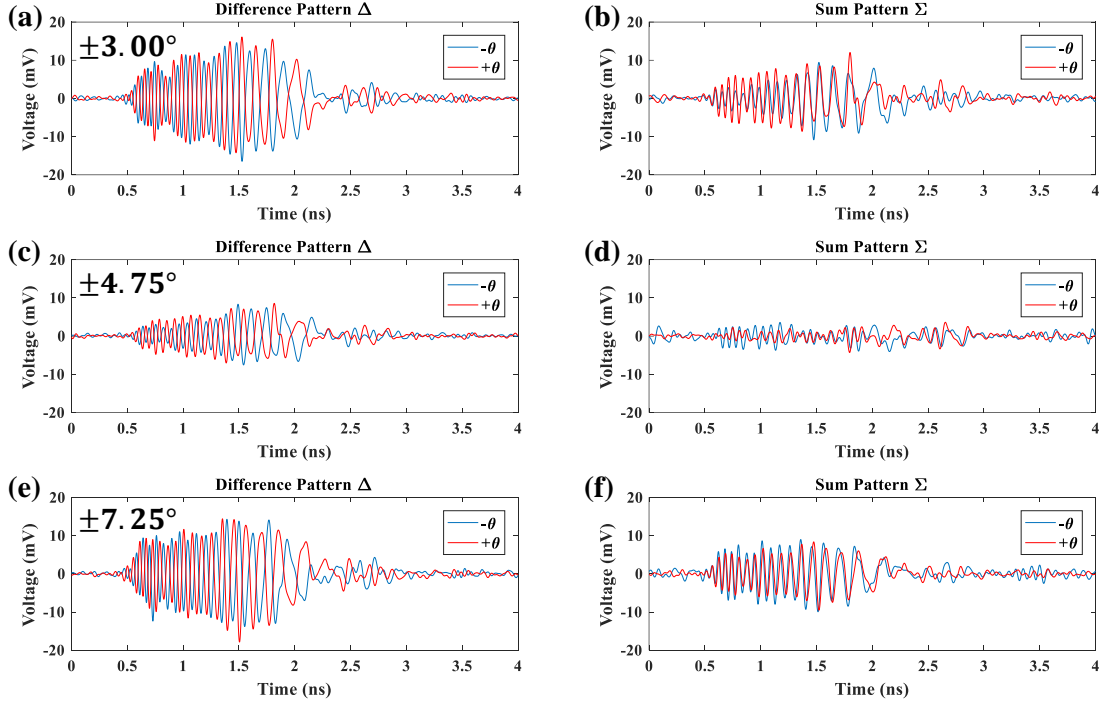
Fig. 4.8: Far-field off-axis antenna time domain waveform measurement. Received waveforms for difference pattern when Tx1 and Tx2 are set out of phase with Rx located with angular offset (a) ±3°, (c) ±4.75° and (e) ±7.25°. Received waveforms for sum pattern when Tx1 and Tx2 are in phase with Rx located with angular offset (b) ±3°, (d) ±4.75° and (f) ±7.25°. Under difference transmission mode, the received waveforms at angular displacements symmetric to center axis have opposite polarities, π phase shift along entire frequency bands. Under sum transmission mode, the two received waveforms at symmetric angular displacements overlap with each other, possessing the same phase feature

When sum transmission mode is switched to difference transmission mode, polarity of second transmitting antenna is flipped while the other transmitting antenna stays unchanged. We have

$$Tx1_{diff}(t) = C(t) \tag{4.5a}$$

$$Tx2_{diff}(t) = -C(t) \tag{4.5b}$$

In the case that the receiving antenna Rx is placed at positive angular displacement $\theta = \theta_+$, the additional arrival time delay for transmitted Tx1 and Tx2 waveforms to

reach Rx comparing to the case that Rx is placed at center axis ($\theta = 0$) is defined as t_1 and t_2, respectively. For the received sum and difference waveforms, we have

$$Rx_{sum}(t, \theta_+) = Rx_{sum}(t, t_1, t_2) = C(t - t_1) + C(t - t_2) \tag{4.6a}$$

$$Rx_{diff}(t, \theta_+) = Rx_{diff}(t, t_1, t_2) = C(t - t_1) - C(t - t_2) \tag{4.6b}$$

When the receiving antenna is placed at negative angular displacement, symmetric to θ_+, we have $\theta = \theta_- = -\theta_+$. The transmitted waveforms Tx1 and Tx2 exchange their arrival delays comparing to θ_+ case. Therefore, the received waveforms can be written as

$$Rx_{sum}(t, \theta_-) = Rx_{sum}(t, t_2, t_1) = C(t - t_2) + C(t - t_1) \tag{4.7a}$$

$$Rx_{diff}(t, \theta_-) = Rx_{diff}(t, t_2, t_1) = C(t - t_2) - C(t - t_1) \tag{4.7b}$$

From Eq. 4.6 and Eq. 4.7, we have

$$Rx_{sum}(t, \theta) = Rx_{sum}(t, -\theta) \tag{4.8a}$$

$$Rx_{diff}(t, \theta) = -Rx_{diff}(t, -\theta) \tag{4.8b}$$

The relation given by Eq. 4.8 is proved in experiment by taking the off-axis waveforms shown in Fig. 4.8. Both sum and difference waveforms are recorded with three symmetric angular displacement pairs. The π phase shift for difference received waveforms can be clearly observed, as well as the overlapping for the sum received waveforms, which is expected.

The off-axis measurement proves the property of the broadband phase shifting on difference transmitted waveforms, in order to acquire the angular displacement in a target detection and remote sensing monopulse-like system with high transverse resolution.

5. ULTRABROAD BAND PHOTONIC W-BAND MONOPULSE RADAR FOR HIGH RESOLUTION TARGET DETECTION

5.1 A Brief Introduction of Monopulse Radar Application

A target can be seen by a radar if it enters the main antenna beam. A search radar normally gives larger error when determining target direction, because it always assumes the target is situated in the direction of center axis of the antenna beam. The straightforward way for tracking is to move the antenna cross the target direction and mark the pointing direction that returns the maximum echo signal. However, such crude method suffers from thermal noise errors and target fluctuation errors (cross-section change of the target). Monopulse radar technique is a better solution to antenna tracking systems, featuring high transverse resolution. Comparing to other tracking systems, such as lobe switching and conical scan, a monopulse system offers several advantages. For example, the monopulse approach is capable of producing a measurement based on a single pulse, so it is immune to echo fluctuation and scintillations. Also, there is no restriction on the pulse repetition rate due the single pulse measurement. Furthermore, the sum channel receives echo at full antenna gain; therefore it does not suffer a crossover loss [66].

In transmission mode, two (or four) feeds are used to generate two (or four) beams at squinted angles. Taking the two-feed case as an example, both feeds will be in phase, as radiation pattern represented by the purple area shown in Fig.5.1, which is called Σ or sum pattern. In reception mode, the antenna pattern is given by the two blue areas in Fig. 5.1. The difference of two received signals is used to estimate the azimuth of the target more exactly. In detail, microwave circuitry is used to process the received signals of both separate antennas. Sum of all feeds Σ (purple
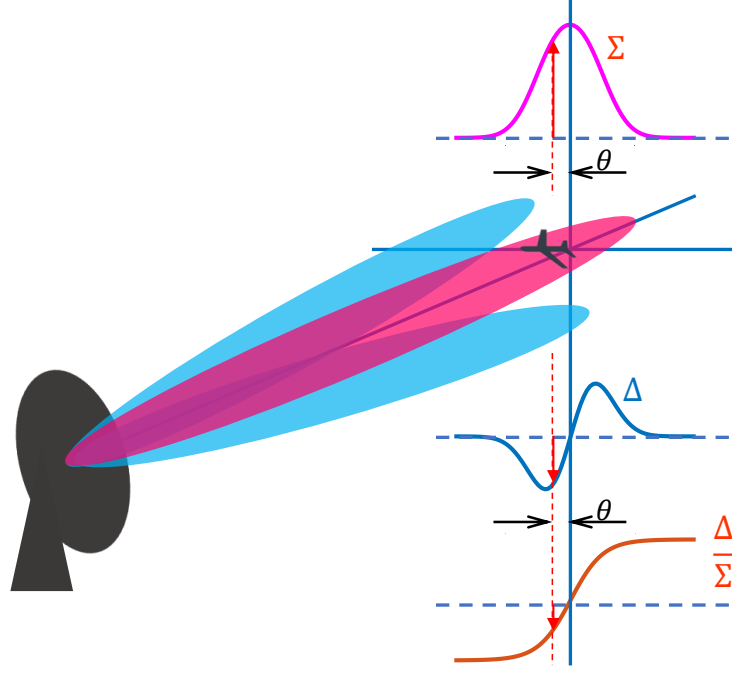
Fig. 5.1: Principle of a monopulse tracking system

trace in Fig.5.1) and difference channels Δ (blue trace in Fig.5.1) will be processed. The output of the difference channels, normalized to the sum channel, is used as an error signal to determine the angular deviation. The sum and difference channels can be expressed as

$$\Sigma(\theta) = G(\theta - \theta_0) + G(\theta + \theta_0) \tag{5.1}$$

$$\Sigma(\theta) = G(\theta - \theta_0) - G(\theta + \theta_0) \tag{5.2}$$

where $G(\theta)$ is the single beam radiation pattern and θ_0 is the squint angle of the individual beam. A four feed monopulse circuitry is shown in Fig. 5.2. The math is similar to two-feed system with an additional degree of freedom, offering precise angular resolution in both elevation and azimuth directions. It subtracts the output of the left pair from the output of the right pair to sense any unbalance in the azimuth
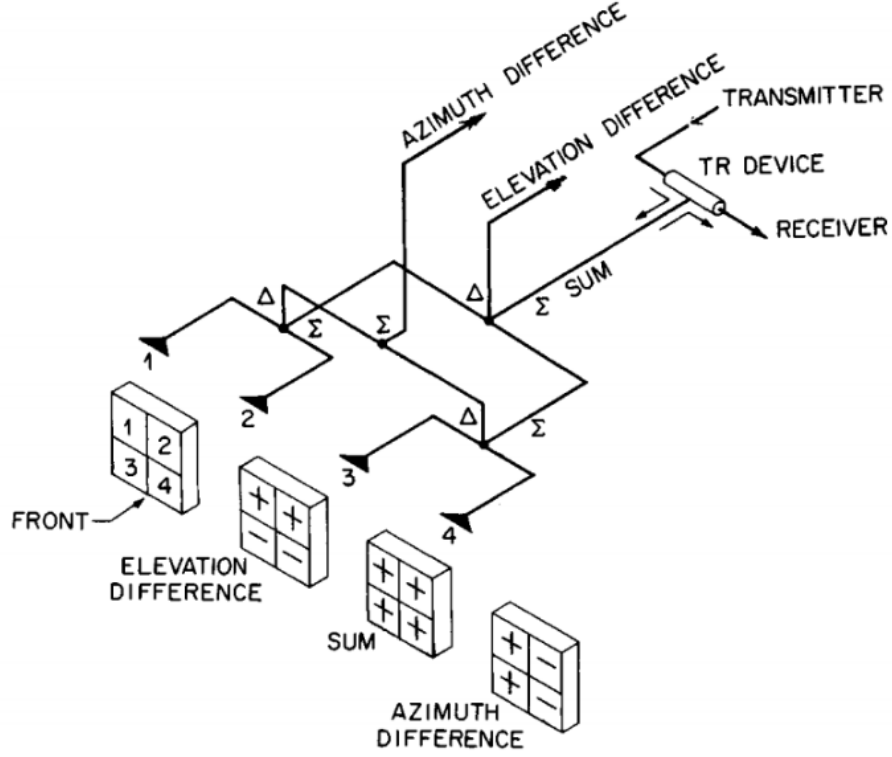
Fig. 5.2: Microwave-comparator circuitry used with a four-horn monopulse fed, adapted from [67]

direction. It also subtracts the output of the top pair from the output of the bottom pair to sense any unbalance in the elevation direction [67].

5.2 Received Waveforms and Compression in Photonic Monopulse-Like Radar Systems

Here, the photonic monopulse-like system discussed in last chapter is applied to achieve target detection. Note that, there is a difference between this photonic monopulse radar system comparing to the traditional monopulse tracking system. Here, different antenna blocks are used as transmitter array and receiver, as shown in Fig. 5.3, instead of using one antenna block and switching between transmission and reception modes. The receiver block shown in Fig. 4.4 is relocated close to the transmitter array, as displayed in Fig. 5.3(a). Now, the mechanical swinging arm is

used to move a target metal plate (4 inch by 4 inch) along the 3-meter radius arch. This target is marked as target 1 in Fig. 5.3(b) and Fig. 5.4(a). A second identical size target marked as target 2 in Fig. 5.3(b) and Fig. 5.4(a) will be placed when testing the system's ability of multi-targets sensing. When target 1 is moving, target 2 will be fixed. High transverse resolution is demonstrated by detecting the angular displacements of the moving target 1 and high ranging resolution is demonstrated by processing the depth displacement between target 1 and target 2. However, all the received waveforms shown in this section are obtained with only target 1 present and target 2 absent. The method and results for multi-targets sensing will be discussed later in this thesis.

Figure 5.4(b) shows the destructive and constructive interference effect when the target is placed at the center axis of the transmitter array (antenna boresight), which corresponds to the results shown in Fig. 4.6 for the center axis time domain waveforms measurement. Also, similar to the off-axis measurement results shown in Fig. 4.8, sum and difference received waveforms at a pair of symmetric angular displacements are shown in Fig. 5.4(c) and 5.4(d). Again, the expected polarity shift in difference received waveforms and overlapping in sum received waveforms can be clearly seen. These results indicate that this photonic monopulse radar system has the ability to detect the angular displacement of a target with high transverse resolution.

In order to perform high depth and transverse resolution target detection, waveform compression is performed to better resolve the target(s). That is, the cross-correlation function of the received waveforms is calculated by applying a reference waveform $x_{ref}(t)$. The compression is first performed to the down-converted waveforms. Here, the reference waveform is generated using the sum echo waveform $Rx_{sum}(t, \theta = 0)$ shown in Fig. 5.4 (b). Note that, a carrier phase shift is needed to optimize the correlation peak because the down-converted waveform cannot preserve the original W-band carrier (20 ps sampling rate for the 50 GS/S realtime scope), and a carrier phase offset will be added to the off-axis down-converted waveforms
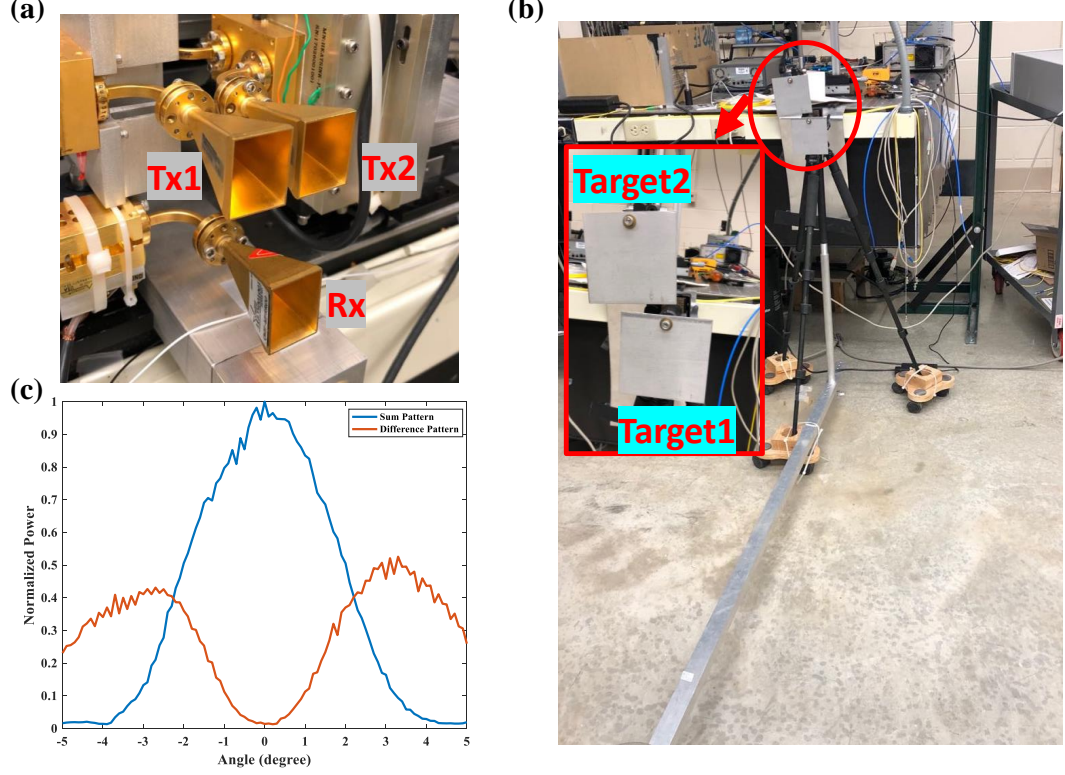
Fig. 5.3: (a) Transmitter and receiver antenna blocks for target detection. Tx1 and Tx2 are separated in horizontal direction with 2 cm. Rx is placed at transmitter array center axis. (b) Targets placed at far-field, 3 meters away to the transmitter and receiver block. (c) Received echo power when transmitter array radiating sum and difference pattern, with only target 1 being place in the far-field, showing similar performance when the receiver is placed at far-field in Fig. 4.7

due to the slight time change or jitter. Here we define $Rx_{sum}(t, \theta = 0) = Re\{\mathbb{X}(t)\}$. Therefore, the reference waveform can be expressed as

$$x_{ref}(t) = Re\{\mathbb{X}(t)e^{\phi(\theta)}\} \tag{5.3}$$

where $\phi(\theta)$ is a carrier phase shift applied, varying with the sum of difference transmission mode and target angular displacement pairs.

Compression results when the target is located at $\pm 3.1°$ are shown in Fig. 5.5. In this case the reference waveform for sum and difference received waveforms can be written as $x_{ref,sum}(t) = Re\{\mathbb{X}(t)e^{\phi_{sum}(\theta=3.1°)}\}$ and $x_{ref,diff}(t) = Re\{\mathbb{X}(t)e^{\phi_{diff}(\theta=3.1°)}\}$.
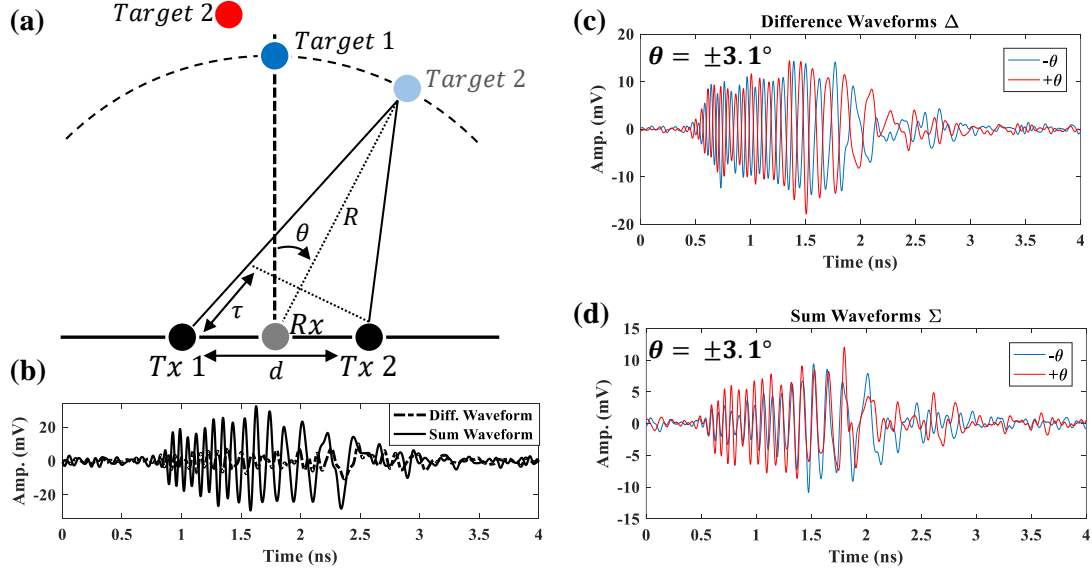
Fig. 5.4: (a) Experimental scheme for target(s) detection. Example received waveforms, (b) received sum and difference waveforms off the reflection from a single target located at center axis, (c) received difference waveforms off the reflection from a single target located at $\pm 3.1°$, and (d) received sum waveforms when the single target is located at $\pm 3.1°$.

After compression, the two compression peaks for sum waveforms are both positive. However, negative peak and positive peak are obtained when using the same difference transmission mode reference waveform for difference received waveforms at plus and minus angular displacement. This indicates the opposite phase feature included in the the difference received waveforms, as expected from the previous analysis in Section 4.4. Compression results with two other angular displacement pairs are also shown here, in Fig. 5.6 and Fig. 5.7. Note that the sign changes on difference compression waveforms preserve and but the amplitudes vary at different angular displacements.
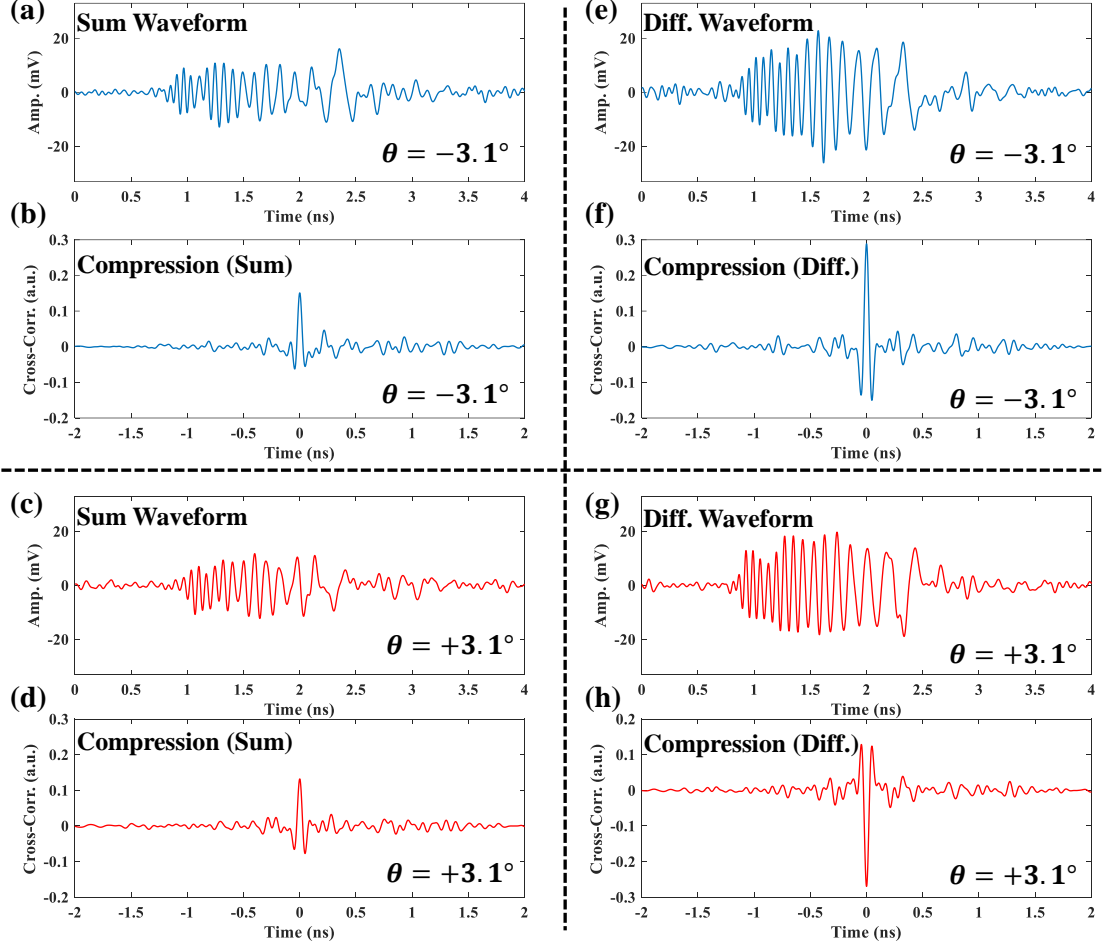
Fig. 5.5: Received sum and difference waveforms and compression at symmetric angular displacement pair ±3.1°. (a) Received sum waveform when the target locates at negative angular displacement; (b) Compression of (a). (c) Received sum waveform when the target locates at positive angular displacement; (d) Compression of (c). (e) Received difference waveform when the target locates at negative angular displacement; (f) Compression of (e). (g) Received difference waveform when the target locates at positive angular displacement; (h) Compression of (g). The correlation peak polarity shift between (f) and (h) indicates the sign difference of the angular displacement.
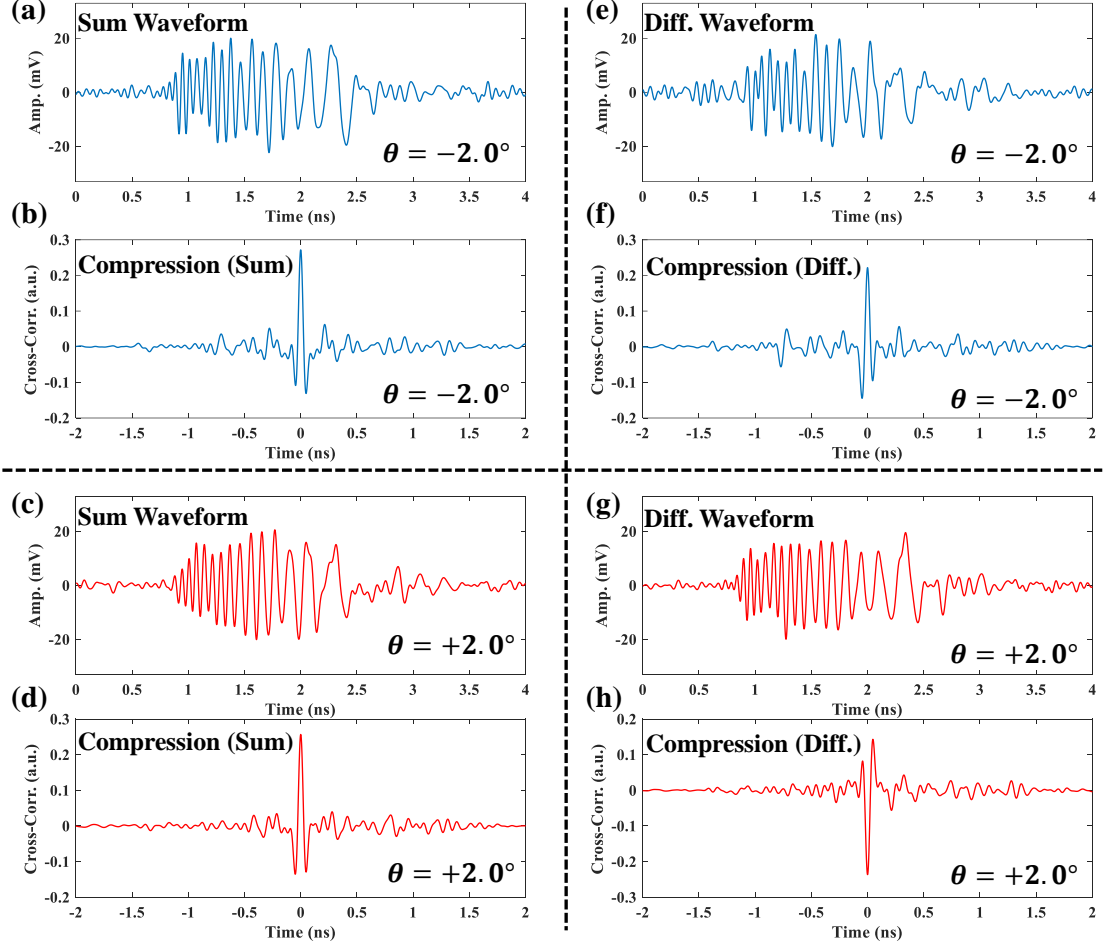
Fig. 5.6: Received sum and difference waveforms and compression at symmetric angular displacement pair ±2.0°. (a) Received sum waveform when the target locates at negative angular displacement; (b) Compression of (a). (c) Received sum waveform when the target locates at positive angular displacement; (d) Compression of (c). (e) Received difference waveform when the target locates at negative angular displacement; (f) Compression of (e). (g) Received difference waveform when the target locates at positive angular displacement; (h) Compression of (g). The correlation peak polarity shift between (f) and (h) indicates the sign difference of the angular displacement.
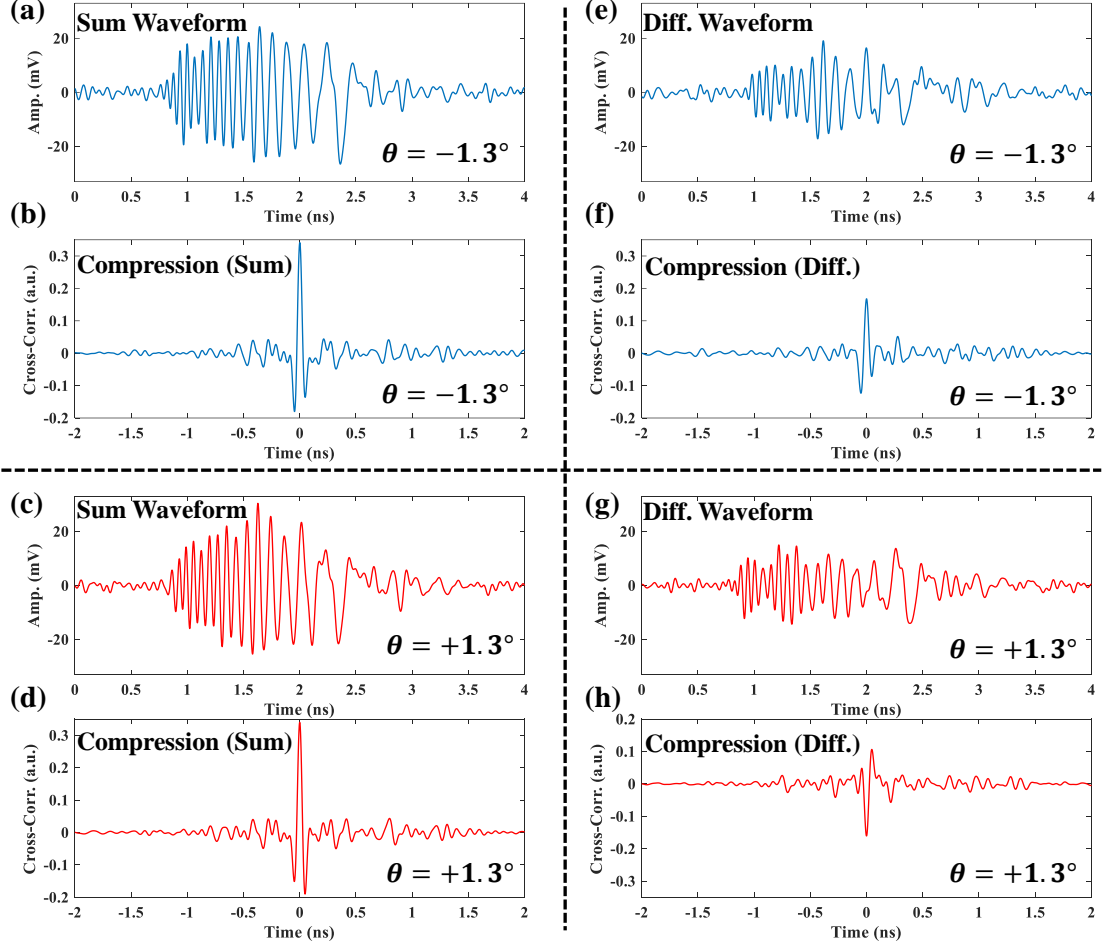
Fig. 5.7: Received sum and difference waveforms and compression at symmetric angular displacement pair ±1.3°. (a) Received sum waveform when the target locates at negative angular displacement; (b) Compression of (a). (c) Received sum waveform when the target locates at positive angular displacement; (d) Compression of (c). (e) Received difference waveform when the target locates at negative angular displacement; (f) Compression of (e). (g) Received difference waveform when the target locates at positive angular displacement; (h) Compression of (g). The correlation peak polarity shift between (f) and (h) indicates the sign difference of the angular displacement.

5.3 Target detection

This system can then be used for remote sensing with high depth and transverse resolution. From Fig. 5.4 (a), under the far-field condition, the radiated waveforms arriving at different times with a difference of Δt at target 1, between waveforms transmitted by Tx1 and waveforms transmitted by Tx2, can be written as

$$\Delta t = \frac{d \sin \theta}{c} \tag{5.4}$$

where d is the distance between two transmitter antennas, θ is the angular displacement, and c is the speed of light. The time period of a 87.5 GHz (waveform carrier frequency in this work) single frequency W-band waveform is 11.43 ps, meaning the 20 ps scope sampling time is not enough to precisely retrieve the target angular displacement information via waveform compression, and that explains why a carrier phase offset has to be added on when generating the reference waveform in order to optimize the compression peaks on the down-converted waveforms. Therefore, in this section, all the waveforms are processed in W-band after reconstruction via up-conversion, including the reference waveforms for compression. The waveforms used to generate reference waveforms are shown in Fig. 5.8. The difference waveforms $Tx1_{diff}(t)$ and $Tx2_{diff}(t)$ are exactly out of phase (π phase shift along the entire broadband chirp waveforms), and the sum waveforms $Tx1_{sum}(t)$ and $Tx2_{sum}(t)$ are in phase. We also have

$$Tx1_{sum} = Tx1_{diff}(t) \tag{5.5a}$$

$$Tx2_{sum} = -Tx2_{diff}(t) \tag{5.5b}$$

Note that the amplitude responses are different for $Tx1(t)$ and $Tx2(t)$ because the two UTC-PD photomixers used here are not identical, as shown in Fig. 5.8. Since the reference waveforms for compression are calculated from the experimental data with such difference in amplitude response, we don't assume $Tx1_{sum}(t) = Tx2_{sum}(t)$ and
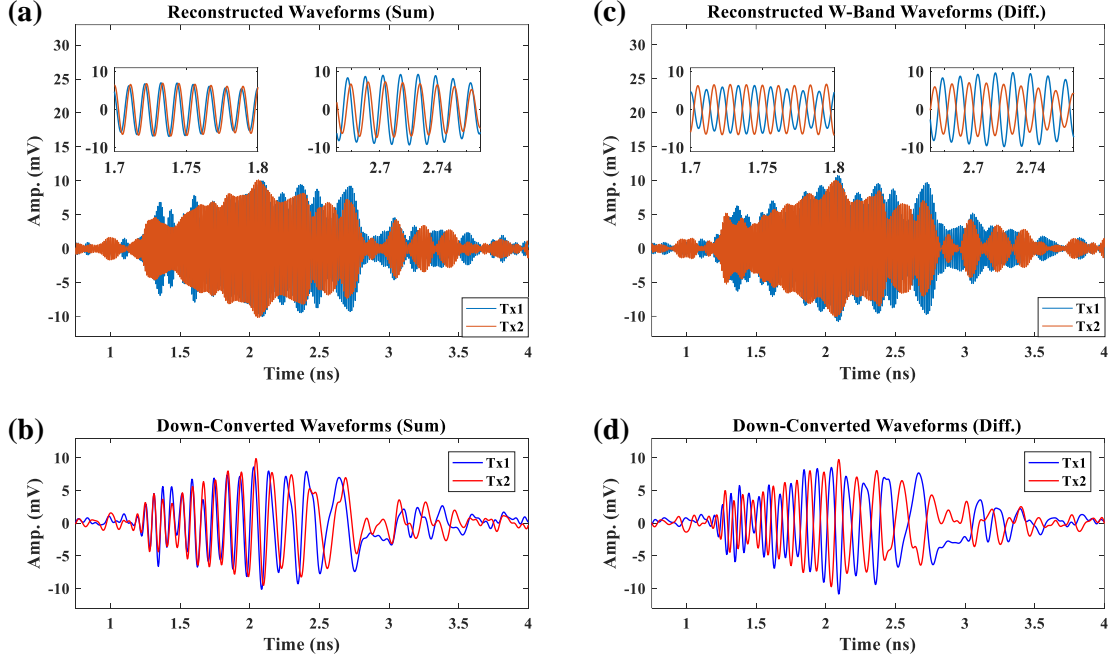
Fig. 5.8: W-band reflected chirp waveforms used to generate reference waveforms for compression. The waveforms are obtained when the target is located at center axis. (a) The reconstructed W-band waveforms $Tx1_{sum}(t)$ and $Tx2_{sum}(t)$ when only a single transmitter antenna is operating under sum transmission mode, the insets show the same polarity on received waveforms from each single transmitter antenna and the waveform chirping; (b) The original down-converted waveforms recorded by the realtime scope and used for up-conversion in (a). (c) The reconstructed W-band waveforms $Tx1_{diff}(t)$ and $Tx2_{diff}(t)$ when only a single transmitter antenna is operating under difference transmission mode, the insets show polarity switch on two waveforms under difference transmission mode; (d) The original down-converted waveforms recorded by the realtime scope and used for up-conversion in (c).

$Tx1_{diff}(t) = -Tx2_{diff}(t)$. The reference waveform used to compress sum received echo waveforms can be written as

$$x_{ref,sum}(t) = Tx1_{sum}(t) + Tx2_{sum}(t) \tag{5.6}$$

it is used to obtain ranging information as shown in the work of [56]. The workhorse for angular displacement detection is a series of difference reference waveforms cal-

culated with respected to the single waveform arriving time difference Δt. These reference waveforms can be written as

$$x_{ref,diff}(t, \Delta t) = Tx1_{diff}(t - \Delta t) + Tx2_{diff}(t) \tag{5.7}$$

As can be seen from Fig. 5.1(a), Eq. 5.4, and Eq. 5.7, when the target angular displacement θ is negative, waveforms radiated by Tx1 arrive before waveforms radiated by Tx2, hence resulting negative arriving time difference Δt. When the target angular shift θ is positive, waveforms from Tx2 arrives first and the sign of Δt is overturned. Because the two transmitted waveforms in difference mode are different (π phase shift), the generated difference reference waveforms are unique with different Δt.

To compress the waveforms in W-band, again cross-correlation calculation is performed here

$$Xcorr_{sum}(\tau) = x_{ref,sum}(t) \star Rx_{sum}(t) \tag{5.8a}$$

$$Xcorr_{diff}(\tau, \Delta t) = x_{ref,diff}(t, \Delta t) \star Rx_{diff}(t) \tag{5.8b}$$

The target detection system is first used to detect a single target. We have the target metal plate (shown in Fig. 5.3(b)) moving along the 3-meter arc, trying to detect the angular displacement. Figure 5.9 shows three example results for the single target detection experiments. In this experiment, via cross-correlation, we apply the difference reference waveforms to compress the received difference waveforms reflected from the target. The angular displacement information can be retrieved based on the Δt_{opt} which furnished the best compression $x_{ref,diff}(t, \Delta t_{opt})$. The three $x_{ref,diff}(t, \Delta t_{opt})$ waveforms are shown in Fig. 5.9(a), Fig. 5.9(c) and Fig. 5.9(e), with the targets located at three different angular position respectively. The corresponding correlation peak value with varying Δt value for reference waveforms is shown in Fig. 5.9(b), Fig. 5.9(d) and Fig. 5.9(f). Δt_{opt} designates the best matching reference waveform to the actual received waveform. Hence, via Eq. 5.4, angular displace-

ment value can be found. The retrieved angular displacement values ($-1.06°$, $-0.65°$, and $+1.91°$) match the angular displacement measured by the mechanical method $\theta_{mechanical}$ ($-1.0°$, $-0.6°$, and $+2.0°$). Fig. 5.10 shows more results of the retrieved angular displacements when the single target is setup at different angular positions by the mechanical arm.
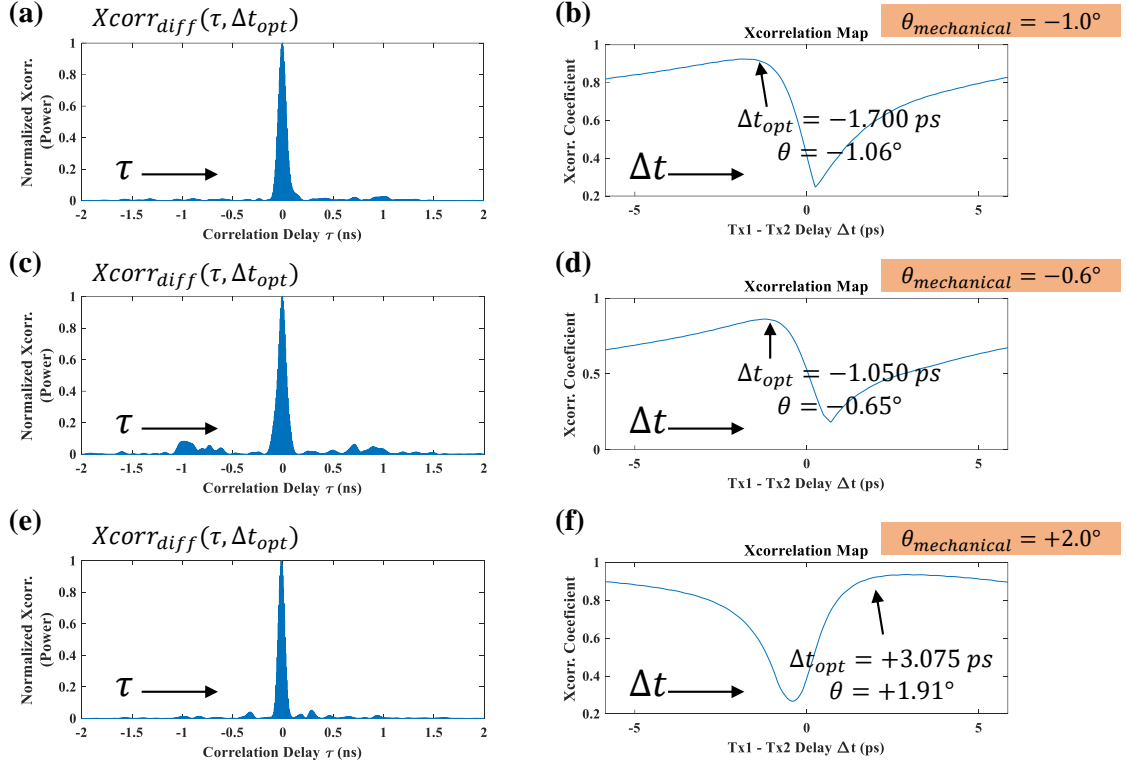
Fig. 5.9: Compression for single target angular displacement sensing, with three angles shown here. (a) Compression using $x_{ref,diff}(t, \Delta t_{opt})$ in W-band when target is at $\theta = -1.06°$. (b) Maximum correlation coefficient with different Δt value of $x_{ref,diff}(t, \Delta t)$. (c) Compression using $x_{ref,diff}(t, \Delta t_{opt})$ in W-band when target is at $\theta = -0.65°$. (d) Maximum correlation coefficient with different Δt value of $x_{ref,diff}(t, \Delta t)$. (e) Compression using $x_{ref,diff}(t, \Delta t_{opt})$ in W-band when target is at $\theta = +1.91°$. (f) Maximum correlation coefficient with different Δt value of $x_{ref,diff}(t, \Delta t)$.

Next, we test the system's ability of detecting multiple targets. As shown in Fig. 5.3 and Fig. 5.4, target 1 can scan along a 3-meter arc with a fixed range and target 2 is fixed when target 1 is moving along the arc. First, compression using cross-correlation is performed to the received sum waveform using sum reference waveform
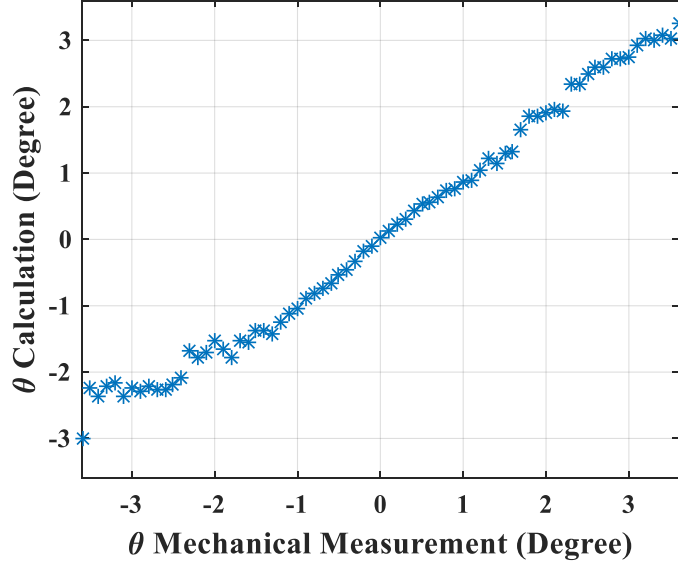
Fig. 5.10: Retrieved angular displacements vs. mechanical angular displacement setup.
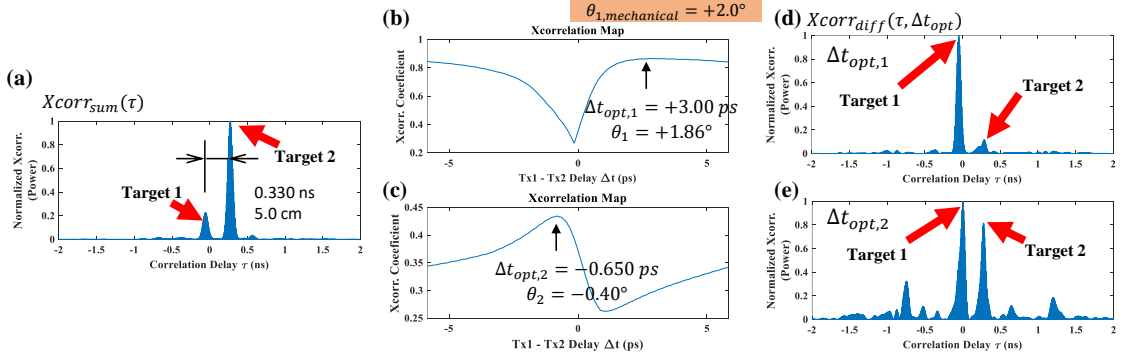
Fig. 5.11: Two targets remote sensing with high depth and transverse resolution. (a) Compression using $x_{ref,sum}(t)$ in W-band for calculating the range difference between the two targets and locating the correlation peak temporal locations of the two targets for angular detection. (b) Maximum correlation coefficient in difference mode with varying Δt value of $x_{ref,diff}(t, \Delta t)$ for target 1. (c) Maximum correlation coefficient in difference mode with varying Δt value of $x_{ref,diff}(t, \Delta t)$ for target 2. (d) Compression using $x_{ref,diff}(t, \Delta t_{opt})$ in W-band and locating the angular displacement of target 1 as $\theta = 1.86°$ (e) Compression using $x_{ref,diff}(t, \Delta t_{opt})$ in W-band and locating the angular displacement of target 2 as $\theta = -0.40°$

.

from Eq. 5.6. The compression result is shown in Fig. 5.11(a). By reading the peak temporal locations, we can calculate the range distance between the two targets, which is 5.0 cm in this example. Since the peak positions will not change when the compression mode is switched from sum mode to difference mode, we can then optimize the two correlation peaks separately in difference mode, using the method discussed in the single-target case. The optimization process of finding Δt_{opt} for each individual target is shown in Fig. 5.11(b) and Fig. 5.11(c). The retrieved angular displacement values for target 1 and target 2 are $+1.86°$ and $-0.40°$ respectively (target 1 is configured at $\theta_{mechanical} = +2.0°$ by the mechanical moving arm). The corresponding $x_{ref,diff}(t, \Delta t_{opt})$ compression waveform in difference mode is shown in Fig. 5.11(d) and Fig. 5.11(e) for target 1 and target 2. respectively. Note that, the peak amplitudes for the same target are different in different compression results, because difference compression waveforms are selected in order to retrieve angular information, but their positions in horizontal axis τ are unchanged. For Fig. 5.11(d), when the peak value of target 1 is optimized, the peak value of target 2 is nearly reduced to the noise value, which is expected as that reflects the angular position difference of the two targets. Furthermore, the method is applied to the entire dataset — two targets with fixed range offset, but target 1 moving along an arc over $\pm 4°$, and target 2 is fixed close to the center axis. The retrieved angle and range information is shown in Fig. 5.12. In each dataset, the fixed target (target 2) shows both constant range and angular displacement and the moving target (target 1) shows constant range but linearly varying angular displacement, corresponding to the angles set by the robotic positioner.

As shown in Fig. 5.13, the closest depth distance achieved by this system is 1.4 cm, roughly corresponding to the 15 GHz waveform bandwidth. Note that in Fig. 5.13(a), when the two targets are 1.4 cm apart in range, we have smaller number of valid total data points. The reason is for some of target 1 and target 2 position points, we cannot clearly resolve two separate correlation peaks after compression, as shown in Fig. 5.13. Hence, 1.4 cm is the system limit in ranging.
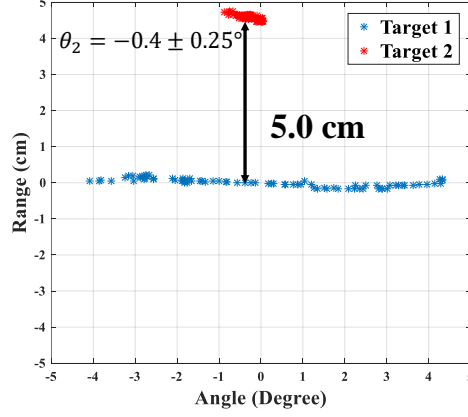
Fig. 5.12: Remote targets sensing with high depth and angular resolution. Two targets have fixed range offset, but target 1 moving along an arc over $\pm 4°$, and target 2 is fixed close to the center axis.
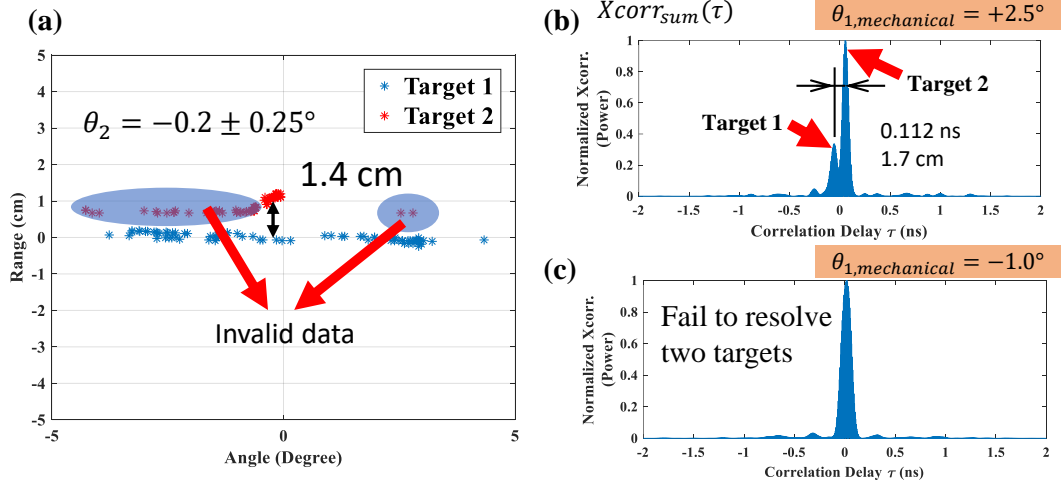
Fig. 5.13: Remote targets sensing with high depth and angular resolution. (a) Two targets have fixed range offset (1.4 cm), but target 1 moving along an arc over $\pm 4°$, and target 2 is fixed close to the center axis. (b) The compression waveform when two targets can be resolved. (c) The compression waveform when the method fail to resolve two compression peaks, hence resulting the invalid data shown in the shadowed area in (a).

In sum, a W-band photonic monopulse-like radar system with ultra-wide bandwidth (80 95 GHz, 1.5 ns time duration) phase shifting is utilized for remote target sensing system with high range ($\pm 0.7 cm$) and transverse resolution ($\pm 0.25°$). We

demonstrate this system for proof-of-principle radar experiments which are able to resolve two targets in range and angle. However, there are some limitations in this 2-D remote sensing approach. Only sum waveform information is applied for ranging and only difference waveform information is applied for angular displacement detection. Such approach limits the system signal to noise performance and also does not fully exploit the information combined in both sum and difference mode. Therefore, the data processing method can be further improved, in order to combine the information from both sum and difference waveforms and improve the system performance.

6. SUMMARY AND FUTURE RESEARCH DIRECTIONS

6.1 Summary

In this work, we experimentally investigated optical and RF signal transmission in complex environments under three different scenarios. Chapter 1 reviewed the previous research milestones for optical imaging and focusing in highly scattering materials, highly scattering multipath RF wireless channel sounding and compensation, and target sensing using millimeter-wave and radar technologies. We also introduced the newly proposed approaches to solve the problems established following the previous research work, focusing in optical spatialtemporal focusing in highly multimode fiber, dynamic channel sounding and compensation with high-speed update rate, and high range and angular resolution sensing using W-band (75-110 GHz) photonic monopulse-like radar system.

In Chapter 2, we demonstrated reference-free characterization of spatial and temporal speckle at varying spatial positions of the output face of a multimode fiber and achieve space-time focusing involving all excited propagating modes. This work further exploit the capacity of multimode fiber, by overcoming and utilizing distortions caused by modal dispersion in a highly multimode fiber. Such distortion can scramble a propagating field in both space and time. While this work is analogous to our groups previous work on temporal shaping of ultrawideband RF wireless signals for temporal and spatial focusing in strong multi-path channels, this work is novel in that it extends the use of pulse shaping for spatial/temporal focusing into the optical regime — highly scattering multimode fiber. Beyond space-time focusing, our system shows the potential to encode the compressed transmitted information for a specific input-output spot, to realize covert sharing in a space-division multiplexed multichannel multimode fiber communication system. Also, with the development of

on-chip pulse shapers, this pulse shaping approach opens possibilities for highly compact shaper-multimode fiber modules, which are not possible with spatial wavefront shaping approaches that fundamentally depend on bulk optic spatial light modulators. There is also potential for application in nonlinear microscopy and imaging.

In Chapter 3, we implemented spread spectrum channel sounding on an electronics processing unit comprising fast analog-to-digital and digital-to-analog converters tightly coupled to a high end FPGA; this approach essentially eliminates latency and communications bottlenecks that are unavoidable with general purpose test equipment such as arbitrary waveform generators and oscilloscopes. In particular, we demonstrated dynamic compensation of a strong multipath RF channel with tens of nanoseconds of delay spread over broad bandwidth (from DC to 6 GHz) with refresh rate as fast as 30 microseconds (a time scale suitable for mobile operation). Characterization and compensation of multipath signal distortion had previously been reported but were slow and limited to static channels. The impact of this work is to demonstrate new opportunities for enhanced performance (signal-to-noise, covertness potential) of mobile or dynamic broadband RF signaling over multipath channels.

In Chapter 4, we demonstrated waveform generation and radar beamforming suitable for W-band (75-110 GHz) chirped monopulse-like radar by using a pair of optical pulse shaping based RF arbitrary waveform generators which drive a pair of high-power uni-traveling carrier photodiode (UTC-PD) based photonic transmitters connected to a pair of standard horn antennas for signal emission. By changing the relative polarity of the drive waveforms, we have achieved constructive (sum transmission mode) and destructive interference (difference transmission mode) of the on-axis radiation with 15 dB average contrast over 80-95 GHz. Far-field antenna array patterns are also acquired, proving the capability of focusing energy in different spatial directions by changing the phase between two broadband transmit waveforms. Comparing to the traditional monopulse tracking radar system with electronic phase shifter under 1 GHz bandwidth, this photonic approach allows phase shifting over entire 15 GHz (bandwidth not limited by optics). The extremely wide-bandwidth

property offers high ranging resolution, in addition to the high transverse resolution monopulse-like sensing system.

Chapter 5 is the continued work from Chapter 4 where we report the two-element transmitter array with arbitrary RF waveform generation. In Chapter 5, a W-band photonic monopulse-like radar system with ultra-wide bandwidth (80 95 GHz, 1.5 ns time duration) phase shifting is utilized for remote target sensing system with high range ($\pm 0.7cm$) and transverse resolution ($\pm 0.25°$). For the first time we demonstrate this system for proof-of-principle radar experiments which are able to resolve two targets in range and angle.

6.2 Future Research Directions

In Chapter 2, we demonstrated spatialtemporal focusing in multimode fiber with single input spot and multiple output spots. An interesting future research direction is to expand the system to multiple input spots. Similar to our groups' previous work [95], which independently compensated several multipath RF channels with multiple inputs and single outputs and overlay all the peaking signal in time to achieve improved signal-to-noise/interference performance, pulses from different multimode fiber input spots can be spatialtemporally focused at the same output spot, resulting in constructively interfered peaking. This can be implemented by either using direct characterization approach as discussed in Chapter 2 or using the reciprocity property. Such multiple-input-multiple-output (MIMO) will further push the communication capability in a space-division multimode fiber communication system. Another interesting research direction in multimode fiber work is to implement it on a photonic-integrated chip. The use of pulse shaping technique and the development of on-chip pulse shapers provide the possibility to make the entire system compact, including everything from laser source to multimode waveguide,

The future direction for the dynamic multipath wireless channel sounding and compensation experiments is to overlay data modulation. In this way, the testbed

would provide a data link in which waveforms matched to the multiply-scattering propagation environment provide processing gain to suppress the effects of interference. We can also further increase the data rate by overlaying the pre-compensation waveforms. Because the pre-compensation waveforms have much longer time duration comparing to the compensation signals, the final peaking signal will be located much closer to each other in time, hence resulting in higher data rate. For example, if 4 ns time period is applied to the pre-compensation waveforms, 250 megabits per seconds can be achieved in this jamming resistance and time varying system. Further modulation scheme can also improve the data rate even more.

For the millimeter-wave photonic radar array sensing experiment, next step will be adding another one or two transmitter antennas in another transverse dimension. By applying the same technique approach as discussed in Chapter 4 and Chapter 5, a 3-D remote sensing system with high depth (range) and transverse (azimuth and elevation) resolution can be achieved. Also, other than a monopulse-like system, a synthetic aperture radar (SAR) approach can also be implemented. This is another possible implementation for high transverse resolution radar imaging. Coupled with the inherit high depth resolution from the ultra-broadband photonic method and the signal processing technique, 3-D high resolution sensing and imaging can also be achieved.

REFERENCES

REFERENCES

[1] M.-G. Di Benedetto, *UWB communication systems: a comprehensive overview.* Hindawi Publishing Corporation, 2006, vol. 5.

[2] A. F. Molisch, *Wireless communications.* John Wiley & Sons, 2012, vol. 34.

[3] A. Dezfooliyan and A. M. Weiner, "Photonic synthesis of high fidelity microwave arbitrary waveforms using near field frequency to time mapping," *Optics express*, vol. 21, no. 19, pp. 22 974–22 987, 2013.

[4] D. R. Dowling, "Acoustic pulse compression using passive phase-conjugate processing," *The Journal of the Acoustical Society of America*, vol. 95, no. 3, pp. 1450–1458, 1994.

[5] A. Derode, P. Roux, and M. Fink, "Robust acoustic time reversal with high-order multiple scattering," *Physical review letters*, vol. 75, no. 23, p. 4206, 1995.

[6] K. B. Smith, A. A. Abrantes, and A. Larraza, "Examination of time-reversal acoustics in shallow water and applications to noncoherent underwater communications," *The Journal of the Acoustical Society of America*, vol. 113, no. 6, pp. 3095–3110, 2003.

[7] J. W. Goodman, *Speckle phenomena in optics: theory and applications.* Roberts and Company Publishers, 2007.

[8] I. M. Vellekoop and A. Mosk, "Focusing coherent light through opaque strongly scattering media," *Optics letters*, vol. 32, no. 16, pp. 2309–2311, 2007.

[9] R. Tyson, *Principles of adaptive optics.* CRC press, 2010.

[10] S. Popoff, G. Lerosey, M. Fink, A. C. Boccara, and S. Gigan, "Image transmission through an opaque material," *Nature Communicaitons*, vol. 1, p. 81, 2010.

[11] S. Popoff, G. Lerosey, R. Carminati, M. Fink, A. Boccara, and S. Gigan, "Measuring the transmission matrix in optics: an approach to the study and control of light propagation in disordered media," *Physical review letters*, vol. 104, no. 10, p. 100601, 2010.

[12] X. Xu, H. Liu, and L. V. Wang, "Time-reversed ultrasonically encoded optical focusing into scattering media," *Nature photonics*, vol. 5, no. 3, pp. 154–157, 2011.

[13] A. P. Mosk, A. Lagendijk, G. Lerosey, and M. Fink, "Controlling waves in space and time for imaging and focusing in complex media," *Nature photonics*, vol. 6, no. 5, pp. 283–292, 2012.

[14] A. M. Weiner, "Ultrafast optics: focusing through scattering media," *Nature Photonics*, vol. 5, no. 6, pp. 332–334, 2011.

[15] M. Webster, K. Webb, and A. Weiner, "Temporal response of a random medium from third-order laser speckle frequency correlations," *Physical review letters*, vol. 88, no. 3, p. 033901, 2002.

[16] J. Bertolotti, E. G. van Putten, C. Blum, A. Lagendijk, W. L. Vos, and A. P. Mosk, "Non-invasive imaging through opaque scattering layers," *Nature*, vol. 491, no. 7423, pp. 232–234, 2012.

[17] O. Katz, E. Small, Y. Bromberg, and Y. Silberberg, "Focusing and compression of ultrashort pulses through scattering media," *Nature photonics*, vol. 5, no. 6, pp. 372–377, 2011.

[18] J. Aulbach, B. Gjonaj, P. M. Johnson, A. P. Mosk, and A. Lagendijk, "Control of light transmission through opaque scattering media in space and time," *Physical review letters*, vol. 106, no. 10, p. 103901, 2011.

[19] D. J. McCabe, A. Tajalli, D. R. Austin, P. Bondareff, I. A. Walmsley, S. Gigan, and B. Chatel, "Spatio-temporal focusing of an ultrafast pulse through a multiply scattering medium," *Nature communications*, vol. 2, p. 447, 2011.

[20] M. Mounaix, D. Andreoli, H. Defienne, G. Volpe, O. Katz, S. Grésillon, and S. Gigan, "Spatiotemporal coherent control of light through a multiple scattering medium with the multispectral transmission matrix," *Physical review letters*, vol. 116, no. 25, p. 253901, 2016.

[21] Y. Choi, C. Yoon, M. Kim, T. D. Yang, C. Fang-Yen, R. R. Dasari, K. J. Lee, and W. Choi, "Scanner-free and wide-field endoscopic imaging by using a single multimode optical fiber," *Physical review letters*, vol. 109, no. 20, p. 203901, 2012.

[22] M. NGom, T. B. Norris, E. Michielssen, and R. R. Nadakuditi, "Mode control in a multimode fiber through acquiring its transmission matrix from a reference-less optical system," *Optics letters*, vol. 43, no. 3, pp. 419–422, 2018.

[23] D. Richardson, J. Fini, and L. E. Nelson, "Space-division multiplexing in optical fibres," *Nature Photonics*, vol. 7, no. 5, p. 354, 2013.

[24] T. Mori, T. Sakamoto, M. Wada, T. Yamamoto, and F. Yamamoto, "Few-mode fibers supporting more than two lp modes for mode-division-multiplexed transmission with mimo dsp," *Journal of Lightwave Technology*, vol. 32, no. 14, pp. 2468–2479, 2014.

[25] H. Defienne, M. Barbieri, I. A. Walmsley, B. J. Smith, and S. Gigan, "Two-photon quantum walk in a multimode fiber," *Science advances*, vol. 2, no. 1, p. e1501054, 2016.

[26] L. G. Wright, Z. Liu, D. A. Nolan, M.-J. Li, D. N. Christodoulides, and F. W. Wise, "Self-organized instability in graded-index multimode fibres," *Nature Photonics*, vol. 10, no. 12, p. 771, 2016.

[27] L. G. Wright, D. N. Christodoulides, and F. W. Wise, "Spatiotemporal mode-locking in multimode fiber lasers," *Science*, vol. 358, no. 6359, pp. 94–97, 2017.

[28] K. Krupa, A. Tonello, B. M. Shalaby, M. Fabert, A. Barthélémy, G. Millot, S. Wabnitz, and V. Couderc, "Spatial beam self-cleaning in multimode fibres," *Nature Photonics*, vol. 11, no. 4, p. 237, 2017.

[29] R. Di Leonardo and S. Bianchi, "Hologram transmission through multi-mode optical fibers," *Optics express*, vol. 19, no. 1, pp. 247–254, 2011.

[30] S. Bianchi and R. Di Leonardo, "A multi-mode fiber probe for holographic micromanipulation and microscopy," *Lab on a Chip*, vol. 12, no. 3, pp. 635–639, 2012.

[31] I. N. Papadopoulos, S. Farahi, C. Moser, and D. Psaltis, "Focusing and scanning light through a multimode optical fiber using digital phase conjugation," *Optics express*, vol. 20, no. 10, pp. 10 583–10 590, 2012.

[32] B. Redding, S. M. Popoff, and H. Cao, "All-fiber spectrometer based on speckle pattern reconstruction," *Optics express*, vol. 21, no. 5, pp. 6584–6600, 2013.

[33] N. Coluccelli, M. Cassinerio, B. Redding, H. Cao, P. Laporta, and G. Galzerano, "The optical frequency comb fibre spectrometer," *Nature communications*, vol. 7, p. 12995, 2016.

[34] R. Rokitski and S. Fainman, "Propagation of ultrashort pulses in multimode fiber in space and time," *Optics express*, vol. 11, no. 13, pp. 1497–1502, 2003.

[35] Z. Guang, M. Rhodes, and R. Trebino, "Measuring spatiotemporal ultrafast field structures of pulses from multimode optical fibers," *Applied Optics*, vol. 56, no. 12, pp. 3319–3324, 2017.

[36] E. E. Morales-Delgado, S. Farahi, I. N. Papadopoulos, D. Psaltis, and C. Moser, "Delivery of focused short pulses through a multimode fiber," *Optics express*, vol. 23, no. 7, pp. 9109–9120, 2015.

[37] E. E. Morales-Delgado, D. Psaltis, and C. Moser, "Two-photon imaging through a multimode fiber," *Optics express*, vol. 23, no. 25, pp. 32 158–32 170, 2015.

[38] A. M. Weiner, "Femtosecond pulse shaping using spatial light modulators," *Review of scientific instruments*, vol. 71, no. 5, pp. 1929–1960, 2000.

[39] ——, "Ultrafast optical pulse shaping: A tutorial review," *Optics Communications*, vol. 284, no. 15, pp. 3669–3692, 2011.

[40] A. Dezfooliyan and A. M. Weiner, "Phase compensation communication technique against time reversal for ultra-wideband channels," *IET Commun*, vol. 7, no. 12, pp. 1287–1295, 2013.

[41] ——, "Experimental investigation of uwb impulse response and time reversal technique up to 12 ghz: Omnidirectional and directional antennas," *IEEE Transactions on Antennas and Propagation*, vol. 60, no. 7, pp. 3407–3415, 2012.

[42] A. Goldsmith, *Wireless communications*. Cambridge university press, 2005.

[43] D. B. Jourdan, D. Dardari, and M. Z. Win, "Position error bound for uwb localization in dense cluttered environments," *IEEE transactions on aerospace and electronic systems*, vol. 44, no. 2, 2008.

[44] A. Dezfooliyan and A. M. Weiner, "Microwave photonics for space–time compression of ultrabroadband signals through multipath wireless channels," *Optics letters*, vol. 38, no. 23, pp. 4946–4949, 2013.

[45] ——, "Evaluation of time domain propagation measurements of uwb systems using spread spectrum channel sounding," *IEEE Transactions on Antennas and Propagation*, vol. 60, no. 10, pp. 4855–4865, 2012.

[46] Y. Li and A. M. Weiner, "Photonic-assisted error-free wireless communication with multipath precompensation covering 2–18 ghz," *Journal of Lightwave Technology*, vol. 34, no. 17, pp. 4154–4161, 2016.

[47] B. Liu, P. Reddy, and A. Weiner, "Photonic-assisted ultra-wideband arbitrary waveform generation with extended time aperture for multipath channel sounding and compensation," in *CLEO: Applications and Technology.* Optical Society of America, 2017, pp. ATu4B–1.

[48] J. Federici and L. Moeller, "Review of terahertz and subterahertz wireless communications," *Journal of Applied Physics*, vol. 107, no. 11, p. 6, 2010.

[49] J.-W. Shi, C.-B. Huang, and C.-L. Pan, "Millimeter-wave photonic wireless links for very high data rate communication," *NPG Asia Materials*, vol. 3, no. 4, p. 41, 2011.

[50] N.-W. Chen, J.-W. Shi, H.-J. Tsai, J.-M. Wun, F.-M. Kuo, J. Hesler, T. W. Crowe, and J. E. Bowers, "Design and demonstration of ultra-fast w-band photonic transmitter-mixer and detectors for 25 gbits/sec error-free wireless linking," *Optics express*, vol. 20, no. 19, pp. 21 223–21 234, 2012.

[51] S. Koenig, D. Lopez-Diaz, J. Antes, F. Boes, R. Henneberger, A. Leuther, A. Tessmann, R. Schmogrow, D. Hillerkuss, R. Palmer *et al.*, "Wireless sub-thz communication system with high data rate," *Nature Photonics*, vol. 7, no. 12, p. 977, 2013.

[52] T. Nagatsuma, S. Horiguchi, Y. Minamikata, Y. Yoshimizu, S. Hisatake, S. Kuwano, N. Yoshimoto, J. Terada, and H. Takahashi, "Terahertz wireless communications based on photonics technologies," *Optics express*, vol. 21, no. 20, pp. 23 736–23 747, 2013.

[53] S. Saponara, F. Giannetti, B. Neri, and G. Anastasi, "Exploiting mm-wave communications to boost the performance of industrial wireless networks," *IEEE Transactions on Industrial Informatics*, vol. 13, no. 3, pp. 1460–1470, 2017.

[54] K. B. Cooper, R. J. Dengler, N. Llombart, T. Bryllert, G. Chattopadhyay, E. Schlecht, J. Gill, C. Lee, A. Skalare, I. Mehdi, and P. H. Siegel, "Penetrating 3-D Imaging at 4- and 25-m Range Using a Submillimeter-Wave Radar," *IEEE Transactions on Microwave Theory Techniques*, vol. 56, pp. 2771–2778, Dec. 2008.

[55] T.-F. Tseng, J.-M. Wun, W. Chen, S.-W. Peng, J.-W. Shi, and C.-K. Sun, "High-depth-resolution 3-dimensional radar-imaging system based on a few-cycle w-band photonic millimeter-wave pulse generator," *Optics express*, vol. 21, no. 12, pp. 14 109–14 119, 2013.

[56] Y. Li, A. Rashidinejad, J.-M. Wun, D. E. Leaird, J.-W. Shi, and A. M. Weiner, "Photonic generation of w-band arbitrary waveforms with high time-bandwidth products enabling 3.9 mm range resolution," *Optica*, vol. 1, no. 6, pp. 446–454, 2014.

[57] R. McMillan, "Terahertz imaging, millimeter-wave radar," in *Advances in sensing with security applications*. Springer, 2006, pp. 243–268.

[58] M. Tonouchi, "Cutting-edge terahertz technology," *Nature photonics*, vol. 1, no. 2, p. 97, 2007.

[59] R. Appleby and R. N. Anderton, "Millimeter-wave and submillimeter-wave imaging for security and surveillance," *Proceedings of the IEEE*, vol. 95, no. 8, pp. 1683–1690, 2007.

[60] W. M. Brown and L. J. Porcello, "An introduction to synthetic-aperture radar," *IEEE spectrum*, vol. 6, no. 9, pp. 52–62, 1969.

[61] M. Skolnik, "Radar handbook, 1536 pp," 1970.

[62] M. Kishida, K. Ohguchi, and M. Shono, "79 ghz-band high-resolution millimeter-wave radar," *FUJITSU Sci. Tech. J*, vol. 51, no. 4, pp. 55–59, 2015.

[63] P. Molchanov, S. Gupta, K. Kim, and K. Pulli, "Short-range fmcw monopulse radar for hand-gesture sensing," in *Radar Conference (RadarCon), 2015 IEEE*. IEEE, 2015, pp. 1491–1496.

[64] K. B. Cooper, R. J. Dengler, N. Llombart, A. Talukder, A. V. Panangadan, C. S. Peay, I. Mehdi, and P. H. Siegel, "Fast high-resolution terahertz radar imaging at 25 meters," in *Terahertz Physics, Devices, and Systems IV: Advanced Applications in Industry and Defense*, vol. 7671. International Society for Optics and Photonics, 2010, p. 76710Y.

[65] S. Wang, K.-H. Tsai, K.-K. Huang, S.-X. Li, H.-S. Wu, and C.-K. C. Tzuang, "Design of x-band rf cmos transceiver for fmcw monopulse radar," *IEEE Transactions on Microwave Theory and Techniques*, vol. 57, no. 1, pp. 61–70, 2009.

[66] N. Levanon, "Radar principles," *New York, Wiley-Interscience, 1988, 320 p.*, 1988.

[67] *Radar handbook*, 2nd ed. New York: McGraw-Hill, 1990.

[68] J. Yao, "Microwave photonics," *Journal of Lightwave Technology*, vol. 27, no. 3, pp. 314–335, 2009.

[69] R. Rotman, M. Tur, and L. Yaron, "True time delay in phased arrays," *Proceedings of the IEEE*, vol. 104, no. 3, pp. 504–518, 2016.

[70] Z. Jiang, C.-B. Huang, D. E. Leaird, and A. M. Weiner, "Optical arbitrary waveform processing of more than 100 spectral comb lines," *Nature Photonics*, vol. 1, no. 8, pp. 463–467, 2007.

[71] S. T. Cundiff and A. M. Weiner, "Optical arbitrary waveform generation," *Nature Photonics*, vol. 4, no. 11, p. 760, 2010.

[72] J. McKinney, D. Leaird, and A. Weiner, "Millimeter-wave arbitrary waveform generation with a direct space-to-time pulse shaper," *Optics Letters*, vol. 27, no. 15, pp. 1345–1347, 2002.

[73] J. Chou, Y. Han, and B. Jalali, "Adaptive rf-photonic arbitrary waveform generator," *IEICE Transactions on Electronics*, vol. 86, no. 7, pp. 1226–1229, 2003.

[74] I. S. Lin, J. D. McKinney, and A. M. Weiner, "Photonic synthesis of broadband microwave arbitrary waveforms applicable to ultra-wideband communication," *IEEE Microwave and Wireless Components Letters*, vol. 15, no. 4, pp. 226–228, 2005.

[75] M. H. Khan, H. Shen, Y. Xuan, L. Zhao, S. Xiao, D. E. Leaird, A. M. Weiner, and M. Qi, "Ultrabroad-bandwidth arbitrary radiofrequency waveform generation with a silicon photonic chip-based spectral shaper," *Nature Photonics*, vol. 4, no. 2, p. 117, 2010.

[76] Y. Li, A. Dezfooliyan, and A. M. Weiner, "Photonic synthesis of spread spectrum radio frequency waveforms with arbitrarily long time apertures," *Journal of Lightwave Technology*, vol. 32, no. 20, pp. 3580–3587, 2014.

[77] A. Rashidinejad and A. M. Weiner, "Photonic radio-frequency arbitrary waveform generation with maximal time-bandwidth product capability," *Journal of Lightwave Technology*, vol. 32, no. 20, pp. 3383–3393, 2014.

[78] F. J. Quinlan, T. M. Fortier, A. Hati, C. W. Nelson, Y. Fu, J. Campbell, S. A. Diddams *et al.*, "Exploiting shot noise correlations in the photodetection of ultrashort optical pulse trains," *Nature Photonics*, vol. 7, 2013.

[79] T. M. Fortier, M. S. Kirchner, F. Quinlan, J. Taylor, J. Bergquist, T. Rosenband, N. Lemke, A. Ludlow, Y. Jiang, C. Oates *et al.*, "Generation of ultrastable microwaves via optical frequency division," *Nature Photonics*, vol. 5, no. 7, pp. 425–429, 2011.

[80] J. Yao, "Photonics for ultrawideband communications," *IEEE Microwave Magazine*, vol. 10, no. 4, 2009.

[81] J.-W. Shi, F.-M. Kuo, and J. E. Bowers, "Design and analysis of ultra-high-speed near-ballistic uni-traveling-carrier photodiodes under a 50-omega load for high-power performance," *IEEE Photonics Technology Letters*, vol. 24, pp. 533–535, 2012.

[82] B. Liu and A. M. Weiner, "Space-time control of broadband light in a multimode fiber," in *CLEO: Science and Innovations*. Optical Society of America, 2018, pp. SF3N–2.

[83] ——, "Space–time focusing in a highly multimode fiber via optical pulse shaping," *Optics letters*, vol. 43, no. 19, pp. 4675–4678, 2018.

[84] J. Gowar, *Optical communication systems*. Prentice-Hall, 1984.

[85] W. Xiong, P. Ambichl, Y. Bromberg, B. Redding, S. Rotter, and H. Cao, "Principal modes in multimode fibers: exploring the crossover from weak to strong mode coupling," *Optics express*, vol. 25, no. 3, pp. 2709–2724, 2017.

[86] S.-D. Yang, A. M. Weiner, K. R. Parameswaran, and M. M. Fejer, "400-photon-per-pulse ultrashort pulse autocorrelation measurement with aperiodically poled lithium niobate waveguides at 1.55 μm," *Optics letters*, vol. 29, no. 17, pp. 2070–2072, 2004.

[87] Z. Kong, C. Bao, O. E. Sandoval, B. Liu, C. Wang, J. A. Jaramillo-Villegas, M. Qi, and A. M. Weiner, "Characterizing pump line phase offset of a single-soliton kerr comb by dual comb interferometry," *arXiv preprint arXiv:1810.08721*, 2018.

[88] Z. Kong, C. Bao, O. Sandoval, B. Liu, M. Qi, and A. M. Weiner, "All-linear phase retrieval of a single-soliton kerr comb," in *CLEO: Science and Innovations*. Optical Society of America, 2018, pp. STh4N–4.

[89] A. Weiner, *Ultrafast optics*. John Wiley & Sons, 2011, vol. 72.

[90] N. K. Fontaine, R. P. Scott, C. Yang, D. J. Geisler, J. P. Heritage, K. Okamoto, and S. Yoo, "Compact 10 ghz loopback arrayed-waveguide grating for high-fidelity optical arbitrary waveform generation," *Optics letters*, vol. 33, no. 15, pp. 1714–1716, 2008.

[91] S. Tahvili, S. Latkowski, B. Smalbrugge, X. J. Leijtens, P. J. Williams, M. J. Wale, J. Parra-Cetina, R. Maldonado-Basilio, P. Landais, M. K. Smit *et al.*, "InP-based integrated optical pulse shaper: demonstration of chirp compensation," *IEEE Photonics Technology Letters*, vol. 25, no. 5, pp. 450–453, 2013.

[92] A. J. Metcalf, H.-J. Kim, D. E. Leaird, J. A. Jaramillo-Villegas, K. A. McKinzie, V. Lal, A. Hosseini, G. E. Hoefler, F. Kish, and A. M. Weiner, "Integrated line-by-line optical pulse shaper for high-fidelity and rapidly reconfigurable rf-filtering," *Optics Express*, vol. 24, no. 21, pp. 23 925–23 940, 2016.

[93] A. Dezfooliyan and A. M. Weiner, "Spatiotemporal focusing of phase compensation and time reversal in ultrawideband systems with limited rate feedback," *IEEE Transactions on Vehicular Technology*, vol. 65, no. 4, pp. 1998–2006, 2016.

[94] B. Liu, J.-M. Wun, N. P. O'Malley, D. Leaird, N.-W. Chen, J.-W. Shi, and A. M. Weiner, "Extremely wide bandwidth microwave photonic phase shifter for w-band chirped monopulse radar," in *Optical Fiber Communication Conference*. Optical Society of America, 2018, pp. Th3G–6.

[95] A. Dezfooliyan and A. M. Weiner, "Experimental test-bed for studying multiple antenna beamforming over ultra wideband channels up to 12 ghz," *IEEE Wireless Communications Letters*, vol. 1, no. 5, pp. 520–523, 2012.

VITA

VITA

Bohao Liu was born in Shijiazhuang, Hebei, China in 1990. He received his B.S. degree in electrical engineering from Harbin Institute of Technology, Harbin, Heilongjiang, China in 2013 and received his M.S. degree in electrical and computer engineering from Purdue University, West Lafayette, IN, USA in 2018. Since 2013, he has been pursuing his Ph.D. degree at Purdue University.

He has been a research assistant in the Ultrafast Optics and Optical Fiber Communications Laboratory since he joined Purdue University. His research interests include ultrafast optics, pulse shaping, multimode fiber, microwave and millimeter-wave photonics, and wideband wireless radio frequency signal transmission.